



Validation of Elemental and Isotopic Abundances in Late-M Spectral Types with the Benchmark HIP 55507 AB System

Jerry W. Xuan¹, Jason Wang², Luke Finnerty³, Katelyn Horstman¹, Simon Grimm⁴, Anne E. Peck⁵, Eric Nielsen⁵, Heather A. Knutson⁶, Dimitri Mawet^{1,7}, Howard Isaacson^{8,9}, Andrew W. Howard¹, Michael C. Liu¹⁰, Sam Walker¹⁰, Mark W. Phillips¹⁰, Geoffrey A. Blake⁶, Jean-Baptiste Ruffio¹, Yapeng Zhang¹, Julie Inglis⁶, Nicole L. Wallack¹¹, Aniket Sanghi¹, Erica J. Gonzales¹², Fei Dai^{1,6}, Ashley Baker¹, Randall Bartos⁷, Charlotte Z. Bond¹³, Marta L. Bryan¹⁴, Benjamin Calvin^{1,3}, Sylvain Cetre¹⁵, Jacques-Robert Delorme¹⁵, Greg Doppmann¹⁵, Daniel Echeverri¹, Michael P. Fitzgerald³, Nemanja Jovanovic¹, Joshua Liberman^{1,16}, Ronald A. López³, Emily C. Martin¹², Evan Morris¹², Jacklyn Pezzato¹, Garreth Ruane⁷, Ben Sappéy¹⁷, Tobias Schofield¹, Andrew Skemer¹², Taylor Venenciano¹⁸, J. Kent Wallace⁷, Ji Wang¹⁹, Peter Wizinowich¹⁵, Yinzi Xin¹, Shubh Agrawal²⁰, Clarissa R. Do Ó¹⁷, Chih-Chun Hsu²¹, and Caprice L. Phillips¹⁹

¹ Department of Astronomy, California Institute of Technology, Pasadena, CA 91125, USA; jxuan@astro.caltech.edu

² Center for Interdisciplinary Exploration and Research in Astrophysics (CIERA) and Department of Physics and Astronomy, Northwestern University, Evanston, IL 60208, USA

³ Department of Physics & Astronomy, 430 Portola Plaza, University of California, Los Angeles, CA 90095, USA

⁴ Center for Space and Habitability, University of Bern, Gesellschaftsstrasse 6, 3012 Bern, Switzerland

⁵ Department of Astronomy, New Mexico State University, P.O. Box 30001, MSC 4500, Las Cruces, NM 88003, USA

⁶ Division of Geological & Planetary Sciences, California Institute of Technology, Pasadena, CA 91125, USA

⁷ Jet Propulsion Laboratory, California Institute of Technology, 4800 Oak Grove Drive, Pasadena, CA 91109, USA

⁸ Department of Astronomy, University of California at Berkeley, CA 94720, USA

⁹ Centre for Astrophysics, University of Southern Queensland, Toowoomba, QLD, Australia

¹⁰ Institute for Astronomy, University of Hawai'i, 2680 Woodlawn Drive, Honolulu, HI 96822, USA

¹¹ Earth and Planets Laboratory, Carnegie Institution for Science, Washington, DC 20015, USA

¹² Department of Physics and Astronomy, University of California, Santa Cruz, CA 95064, USA

¹³ UK Astronomy Technology Centre, Royal Observatory, Edinburgh EH9 3HJ, UK

¹⁴ David A. Dunlap Institute Department of Astronomy & Astrophysics, University of Toronto, 50 St. George Street, Toronto, ON M5S 3H4, Canada

¹⁵ W.M. Keck Observatory, 65-1120 Mamalahoa Highway, Kamuela, HI, USA

¹⁶ James C. Wyant College of Optical Sciences, University of Arizona, Meinel Building, 1630 East University Boulevard, Tucson, AZ 85721, USA

¹⁷ Center for Astrophysics and Space Sciences, University of California, San Diego, La Jolla, CA 92093, USA

¹⁸ Physics and Astronomy Department, Pomona College, 333 North College Way, Claremont, CA 91711, USA

¹⁹ Department of Astronomy, The Ohio State University, 100 West 18th Avenue, Columbus, OH 43210, USA

²⁰ Department of Physics and Astronomy, University of Pennsylvania, Philadelphia, PA 19104, USA

²¹ Center for Interdisciplinary Exploration and Research in Astrophysics (CIERA), Northwestern University, 1800 Sherman, Evanston, IL 60201, USA

Received 2023 October 6; revised 2023 November 30; accepted 2023 December 3; published 2024 February 1

Abstract

M dwarfs are common host stars to exoplanets but often lack atmospheric abundance measurements. Late-M dwarfs are also good analogs to the youngest substellar companions, which share similar $T_{\text{eff}} \sim 2300\text{--}2800$ K. We present atmospheric analyses for the M7.5 companion HIP 55507 B and its K6V primary star with Keck/KPIC high-resolution ($R \sim 35,000$) K -band spectroscopy. First, by including KPIC relative radial velocities between the primary and secondary in the orbit fit, we improve the dynamical mass precision by 60% and find $M_B = 88.0_{-3.2}^{+3.4} M_{\text{Jup}}$, putting HIP 55507 B above the stellar–substellar boundary. We also find that HIP 55507 B orbits its K6V primary star with $a = 38_{-3}^{+4}$ au and $e = 0.40 \pm 0.04$. From atmospheric retrievals of HIP 55507 B, we measure $[\text{C}/\text{H}] = 0.24 \pm 0.13$, $[\text{O}/\text{H}] = 0.15 \pm 0.13$, and $\text{C}/\text{O} = 0.67 \pm 0.04$. Moreover, we strongly detect ^{13}C (7.8σ significance) and tentatively detect H_2^{18}O (3.7σ significance) in the companion's atmosphere and measure $^{12}\text{CO}/^{13}\text{CO} = 98_{-22}^{+28}$ and $\text{H}_2^{16}\text{O}/\text{H}_2^{18}\text{O} = 240_{-80}^{+145}$ after accounting for systematic errors. From a simplified retrieval analysis of HIP 55507 A, we measure $^{12}\text{CO}/^{13}\text{CO} = 79_{-16}^{+21}$ and $\text{C}^{16}\text{O}/\text{C}^{18}\text{O} = 288_{-70}^{+125}$ for the primary star. These results demonstrate that HIP 55507 A and B have consistent $^{12}\text{C}/^{13}\text{C}$ and $^{16}\text{O}/^{18}\text{O}$ to the $< 1\sigma$ level, as expected for a chemically homogeneous binary system. Given the similar flux ratios and separations between HIP 55507 AB and systems with young substellar companions, our results open the door to systematically measuring ^{13}C and H_2^{18}O abundances in the atmospheres of substellar or even planetary-mass companions with similar spectral types.

Unified Astronomy Thesaurus concepts: Atmospheric composition (2120); Stellar atmospheres (1584); Isotopic abundances (867); Radial velocity (1332)

1. Introduction

The elemental abundances of exoplanets and substellar companions encode their accretion history, providing valuable insights into planet and star formation mechanisms. It is now well recognized that measuring abundance ratios besides C/O

are crucial for breaking degeneracies and providing a more complete picture of substellar atmospheres (e.g., Cridland et al. 2020; Turrini et al. 2021; Mollière et al. 2022; Chachan et al. 2023) when compared to abundance measurements of their host stars. Recently, isotopologue ratios have also emerged as an observable in substellar atmospheres (Mollière & Snelten 2019; Morley et al. 2019). Zhang et al. (2021a) measured $^{12}\text{CO}/^{13}\text{CO} = 31_{-10}^{+17}$ for the young super-Jupiter TYC 8998-760-1 b, while Line et al. (2021) reported $^{12}\text{CO}/^{13}\text{CO} = 10.2\text{--}42.6$ for the hot Jupiter WASP-77 Ab. Finnerty et al. (2023) also reported a tentative ^{13}CO enrichment for WASP-33 b, although higher signal-to-noise ratio (S/N) data are needed to confirm this result. On the other hand, Zhang et al. (2021b) reported $^{12}\text{CO}/^{13}\text{CO} = 97_{-17}^{+25}$ for an isolated brown dwarf. These results potentially indicate that the varying $^{12}\text{C}/^{13}\text{C}$ of these objects can be used to constrain their formation histories. However, more analysis and measurements are required to bolster our confidence in these results (Line et al. 2021).

There are abundant measurements of isotopologues in the stellar literature, especially for giant stars. More recently, studies have measured isotopologue ratios in dwarf stars (e.g., Crossfield et al. 2019; Botelho et al. 2020; Coria et al. 2023), which are thought to better preserve the initial isotopic abundances in their envelopes compared to giant stars and are therefore useful for constraining galactic chemical evolution (Romano et al. 2017). For context, the Sun has $^{12}\text{C}/^{13}\text{C} = 93.5 \pm 3.1$ and $^{16}\text{O}/^{18}\text{O} = 525 \pm 21$ (Lyons et al. 2018), while the average local interstellar medium values are $^{12}\text{C}/^{13}\text{C} = 69 \pm 6$ and $^{16}\text{O}/^{18}\text{O} = 557 \pm 30$ (Wilson 1999). In circumstellar disks, the relative isotopic abundances can differ from the inherited interstellar medium values due to processes such as self-shielding. For example, Calahan et al. (2022) showed that in certain regions of the inner disk, self-shielding of CO and C^{18}O and UV shielding of H_2O can result in an enhanced H_2^{18}O abundance at the expense of C^{18}O . In Zhang et al. (2021a), the authors proposed that ices beyond the CO snow line may be ^{13}CO -rich, so if a planet accreted a significant amount of ice beyond the CO snow line it may exhibit a lower $^{12}\text{CO}/^{13}\text{CO}$ value compared to its host star. However, more detailed modeling work is needed to understand the details of isotopic composition and fractionation chemistry in circumstellar disks (Öberg et al. 2023).

In this work, we study the HIP 55507 AB system, which consists of a M7.5 companion that orbits ~ 40 au from its K6V primary star. The M dwarf companion was initially identified from a radial velocity (RV) trend and later confirmed by adaptive optics imaging (Gonzales et al. 2020). Using *K*-band high-resolution ($R \sim 35,000$) spectra from Keck/KPIC, we carry out an atmospheric retrieval analysis of HIP 55507 B to measure the C/O, [C/H], $^{12}\text{CO}/^{13}\text{CO}$, and $\text{H}_2^{16}\text{O}/\text{H}_2^{18}\text{O}$ in its atmosphere. In addition, we analyze the KPIC spectra of the primary star, HIP 55507 A, to measure its $^{12}\text{CO}/^{13}\text{CO}$ and $\text{C}^{16}\text{O}/\text{C}^{18}\text{O}$ using a simplified version of the same framework.

From the high-resolution spectra, we also measure the RVs of both stars to compute their relative RV. Relative RV data have been shown to improve orbital constraints for directly imaged companions, especially when the other data only sparsely cover the orbital period (Schwarz et al. 2016; Ruffio et al. 2019; Do Ó et al. 2023). We include the KPIC relative RVs in orbit fits to measure the companion’s orbital parameters and dynamical mass.

This paper is organized as follows. In Section 2, we describe the properties of HIP 55507 A, including an estimate of its age. The Keck/HIRES, Keck/NIRC2, and Keck/KPIC observations and data reduction are detailed in Section 3. In Section 4, we summarize the orbit fits for HIP 55507 B. Section 5 lays out our spectral analysis framework for both HIP 55507 A and B, including the retrieval setup. Section 6 describes the lessons from our injection-recovery tests for atmospheric retrievals of HIP 55507 B. The main results of our spectral analysis are described in Section 7, with our conclusions in Section 8.

2. Primary Star Properties

HIP 55507 A is a K6V star located at 25.41 pc with $M = 0.67 \pm 0.02 M_{\odot}$ and $T_{\text{eff}} = 4250 \pm 90$ K (Yee et al. 2017; Stassun et al. 2019; Sebastian et al. 2021; Anders et al. 2022). By comparing the star’s Keck/HIRES optical spectra with an empirical spectral library using the `SpecMatch-Emp` tool (Yee et al. 2017), we obtain $[\text{Fe}/\text{H}] = -0.02 \pm 0.09$ for the star.²² We tabulate the literature properties of HIP 55507 A in Table 1. HIP 55507 A hosts a low-mass companion first detected from RV and direct imaging as part of the TRENDS survey (Gonzales et al. 2020).

We estimated the age of HIP 55507 A in two ways. First, we searched for lithium with the ARC Echelle Spectrograph (Wang et al. 2003) at the Apache Point Observatory 3.5 m on 2023 April 30. The spectrum was reduced with `pyvista`.²³ The spectrum is placed at rest wavelengths by applying a barycentric correction and removing the RV measured by Gaia DR2 (Gaia Collaboration et al. 2018). No Li absorption is visible at 6707.79 Å above the noise, and we determine an upper limit of 20 mÅ on the lithium equivalent width (EW) by constructing a series of Li lines with Gaussian profiles of varying EWs. With this EW upper limit, we place a lower limit on the stellar age using BAFPLES (Stanford-Moore et al. 2020), which uses a Bayesian framework to calculate probability distributions on stellar age for single stars based on Li EW measurements of stars in stellar associations with robust ages. BAFPLES can derive a probability distribution function for a field star given an upper limit on Li EW by using fits to the median Li EW as a function of $B - V$ for each cluster and the scatter about those relations. Given a Li EW upper limit of 20 mÅ and $B - V = 1.24$ for HIP 55507 A, we find 2σ and 3σ lower age limits of 838 and 286 Myr, respectively (see Figure 1).

We also searched TESS light curves for rotational modulation using the `lightkurve` package (Lightkurve Collaboration et al. 2018). HIP 55507 A was observed over two consecutive TESS sectors covering a baseline of 57 days. From the light curves, we found a clear periodic signal of 15.8 days (see Figure 1). Nearby stars within 15’ do not exhibit similar modulation, suggesting the modulation likely originates from HIP 55507 A. If we attribute the periodic signal to the stellar rotation period, a Lomb–Scargle analysis of the two TESS sectors yields a period of 15.8 ± 1.8 days. Given $T_{\text{eff}} = 4250 \pm 90$ K, we use the gyrochronology tool from Bouma et al. (2023) to derive an age of $1.7_{-0.7}^{+0.4}$ Gyr. Therefore, both the lack of Li and relatively slow rotation point to an age of $\sim 1\text{--}2$ Gyr for HIP 55507 A.

²² The error bar of 0.09 dex comes from the rms difference between the measured [Fe/H] of stars in the spectral library and their derived [Fe/H] from `SpecMatch-Emp`. It is the recommended uncertainty to adopt when using `SpecMatch-Emp` (Yee et al. 2017).

²³ <https://pyvista.readthedocs.io/en/latest/index.html>

Table 1
Properties of HIP 55507 AB

Property	Value	References
HIP 55507 A		
$\alpha_{2000.0}$	11:22:05.75	(1)
$\delta_{2000.0}$	+46:54:30.2	(1)
π^a (mas)	39.35 ± 0.015	(1)
Distance (pc)	25.41 ± 0.02	(1)
$\mu_\alpha \cos \delta$ (mas yr ⁻¹)	-197.49 ± 0.01	(1)
μ_δ (mas yr ⁻¹)	-134.78 ± 0.01	(1)
SpT	K6V	(4)
Gaia <i>G</i> (mag)	9.271 ± 0.003	(1)
<i>J</i> (mag)	7.367 ± 0.021	(6)
<i>H</i> (mag)	6.760 ± 0.042	(6)
<i>K_s</i> (mag)	6.613 ± 0.021	(6)
<i>W1</i> (mag)	6.544 ± 0.075	(7)
<i>W2</i> (mag)	6.553 ± 0.023	(7)
Age (Gyr)	$1.7^{+0.4}_{-0.7}$	This paper
Mass ^b (M_\odot)	0.67 ± 0.02	(2), (3), (4), (5)
Literature T_{eff} (K)	4250 ± 90	(2), (3), (5)
Literature $\log g$ (dex)	4.58 ± 0.06	(3), (4), (5), (8)
Literature $v \sin i$ (km s ⁻¹)	3.0 ± 1.0	(5)
T_{eff} (K)	4200 ± 50	This paper
$\log g$ (dex)	4.40 ± 0.25	This paper
P_{rot} (days)	15.8 ± 1.8	This paper
[Fe/H]	-0.02 ± 0.09	This paper
¹² CO/ ¹³ CO	79^{+21}_{-16}	This paper
C ¹⁶ O/C ¹⁸ O	288^{+125}_{-70}	This paper
HIP 55507 B		
SpT	M7.5	This paper
Mass (M_{Jup})	$88.0^{+3.4}_{-3.2}$	This paper
$v \sin i$ (km s ⁻¹)	5.50 ± 0.25	This paper
[C/H]	0.24 ± 0.13	This paper
[O/H]	0.15 ± 0.13	This paper
C/O	0.67 ± 0.04	This paper
¹² CO/ ¹³ CO	98^{+28}_{-22}	This paper
H ₂ ¹⁶ O/H ₂ ¹⁸ O	240^{+145}_{-80}	This paper

Notes.

^a We correct for the DR3 parallax zero-point following the guidelines in Lindegren et al. (2021).

^b The literature values for the stellar mass, T_{eff} , and $\log g$ agree reasonably well, so we take the weighted average from the more recent papers and adopt the standard deviation of the different values as the uncertainty for each parameter.

References. (1) Gaia Collaboration et al. (2023), (2) Sebastian et al. (2021), (3) Stassun et al. (2019), (4) Petigura (2015), (5) Anders et al. (2022), (6) Cutri et al. (2003), (7) Cutri et al. (2021), (8) Foesneau et al. (2022), (9) Yee et al. (2017).

3. Observations and Data Reduction

3.1. Keck/HIRES

We collected spectra of HIP 55507 A from 2009 April to 2023 June using the High Resolution Echelle Spectrometer (HIRES; $R \approx 60,000$; Vogt et al. 1994) at the W.M. Keck Observatory. The data from 2009 to 2015 were collected as part of the M2K program (Gaidos et al. 2013). The observation setup is the same as that used by the California Planet Search (Howard et al. 2010). The wavelength calibration was computed using an iodine gas cell in the light path. A iodine-free template spectrum bracketed by observations of rapidly rotating B-type stars was used to deconvolve the stellar spectrum from the spectrograph point-spread function (PSF). We then forward model the spectra taken

with the iodine cell using the deconvolved template spectra, the PSF model, and the iodine cell line atlas (Butler et al. 1996). The Keck/HIRES RVs are presented in Appendix A and show a long-term trend with curvature, which is induced by HIP 55507 B (Appendix B).

3.2. Keck/NIRC2

We observed HIP 55507 B in the L' band on UT 2021 May 19 and the K and M_s bands on UT 2022 June 9 using Keck/NIRC2. We did not use a focal plane mask but observed in pupil-tracking mode to exploit sky rotation for angular differential imaging (ADI; Liu 2004; Marois et al. 2006). HIP 55507 B was also imaged with Keck/NIRC2 on UT 2012 January 7 and 2015 May 29 (PI: Justin Crepp) as part of the TRENDS survey (Gonzales et al. 2020). The astrometry from Gonzales et al. (2020) shows a $\sim 100^\circ$ discrepancy in position angle (PA) compared to calibrated images in the Keck Observatory Archive,²⁴ which could be caused by a mismatch between the pupil- and field-tracking modes used in each observation (E. Gonzales 2023, private communication). Therefore, we reanalyzed the archival NIRC2 data from Gonzales et al. (2020) to update the astrometry. Finally, we include a single astrometric epoch from UT 2021 December 21 reported in Franson et al. (2023).

We first preprocess the data using the Vortex Imaging Processing software package (Gomez Gonzalez et al. 2017; Christiaens et al. 2023). We perform flat-fielding and bad-pixel removal and correct for geometric distortions by applying the solution in Service et al. (2016) for observations after the NIRC2 camera and adaptive optics system were realigned on UT 2015 April 13 and the solution from Yelda et al. (2010) for the archival 2012 observation. Then, we perform sky subtraction following the procedure described in Xuan et al. (2018). To register the HIP 55507 B frames, we identify the star's position by fitting a 2D Gaussian to the stellar PSF in each frame.

After obtaining the preprocessed cubes, we extracted the astrometry and photometry of the companion using pyKLIP (Wang et al. 2015), which models a stellar PSF with Karhunen-Loève image processing following the framework in Soummer et al. (2012) and Pueyo (2016). We used ADI to subtract the stellar PSF and tested various model choices to minimize the residuals after stellar PSF subtraction while preserving the companion signal, following guidelines in Redai et al. (2023). The 2015 observations for HIP 55507 used field-tracking mode, so we used a least-squares minimization code to compute the astrometry. We note that our measured astrometry from the archival Gonzales et al. (2020) data agree at the $< 1\sigma$ level with those reported in Franson et al. (2023), who also reanalyzed these data.

From pyKLIP forward modeling (Wang et al. 2016), we obtain the flux ratio between the star and companion for each photometric band, which we convert to apparent and absolute magnitudes. For the L' and M_s bands, we scale the flux ratios to the primary star's $W1$ and $W2$ mag, respectively.²⁵ We convert the Two Micron All Sky Survey (2MASS) K into Mauna Kea Observatories (MKO) K for HIP 55507 A using the color

²⁴ <https://koa.ipac.caltech.edu/cgi-bin/KOA/nph-KOALogin>

²⁵ We assume the stars have $L' - W1 = 0$ and $M'_s - W2 = 0$, as these photometric bands are in the Rayleigh-Jeans tail of the spectral energy distribution for HIP 55507 A.

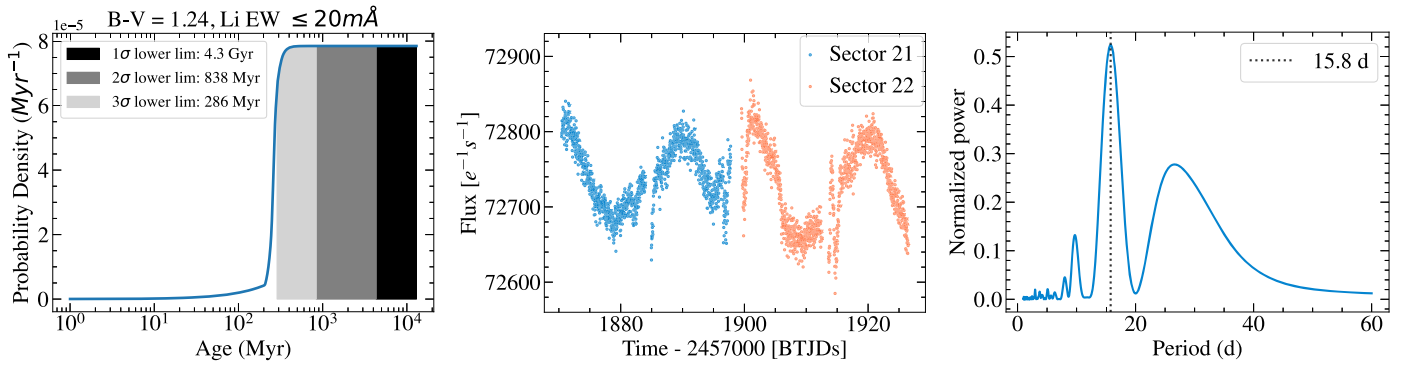


Figure 1. Left: the posterior probability distribution function for the age of HIP 55507 A from BAFFLES (solid blue line), given a lithium EW upper limit of $20 \text{ m}\text{\AA}$ and $B - V = 1.24$. The different shaded regions are 1σ , 2σ , and 3σ lower limits for the age. Middle: TESS light curves from Sectors 21 and 22 extracted from the lightcurve package showing periodic modulation. Right: interpreting this as rotational modulation, a Lomb–Scargle periodogram shows a rotation period of 15.8 ± 1.8 days. The uncertainties on the rotation period were determined from the FWHM of the peak. These two lines of evidence both point toward an age of $\approx 1\text{--}2$ Gyr for the star.

Table 2
NIRC2 Astrometry and Photometry for HIP 55507 B

Time (JD–2400000)	UT Date	Filter	Sep. (mas)	PA (deg)	Δm	m	M_{abs}	References
55934.1	2012-01-07 ^a	H	475.6 ± 3.0	292.33 ± 0.36	(1)
55934.1	2012-01-07 ^a	K'	475.6 ± 3.0	292.50 ± 0.36	(1)
57171.7	2015-05-29 ^a	K_{cont}	550.7 ± 3.0	274.93 ± 0.40	(1)
59353.7	2021-05-19	L'	732.0 ± 3.0	254.75 ± 0.24	4.75 ± 0.01	11.29 ± 0.08	9.27 ± 0.08	(2)
59569.7	2021-12-21 ^b	K_s	748 ± 5	254.04 ± 0.20	(3)
59739.7	2022-06-09	M_s	773.1 ± 5.0	252.04 ± 0.40	4.99 ± 0.05	11.54 ± 0.06	9.52 ± 0.06	(2)
59739.7	2022-06-09	K	767.0 ± 3.1	252.30 ± 0.23	5.07 ± 0.03	11.66 ± 0.04	9.63 ± 0.04	(2)
60034.96	2023-03-31	K	789.9 ± 3.0	250.96 ± 0.40	5.05 ± 0.05	11.64 ± 0.04	9.61 ± 0.05	(2)

Notes.

^a We reanalyzed the data from these epochs to revise the astrometry. The photometry measurements from these epochs are unreliable due to occultation of the central star by the Lyot Coronagraph.

^b This epoch is from Franson et al. (2023), who did not quote photometry.

References. (1) Gonzales et al. (2020), (2) this paper, (3) Franson et al. (2023).

Table 3
KPIC Observations of HIP 55507 AB

UT Date	Target	Exposure Time (minute)	Air Mass	Throughput	Median S/N pixel ⁻¹	Science Fibers
2021 Jul 4	HIP 55507 A	2	1.4	1.1%	150	2, 3
2021 Jul 4	HIP 55507 B	40	1.4	1.1%	10.6	2, 3
2023 May 2	HIP 55507 A	4	1.1	4.6%	225	2, 3
2023 May 2	HIP 55507 B	30	1.1	4.6%	22.3	2, 3

Note. The throughput is end-to-end throughput measured from the top of the atmosphere and varies with wavelength due to differential atmospheric refraction and the instrumental blaze function. The throughput is computed using the HIP 55507 A spectra using its 2MASS $K_s = 6.613$ (Cutri et al. 2003). We report the 95th percentile throughput over the K band, averaged over all frames. The median spectral S/N per pixel from 2.29 to 2.49 μm is also reported.

relations in Leggett et al. (2006) before calculating the MKO K for HIP 55507 B. The measured astrometry and photometry are provided in Table 2, and an example of the pyKLIP forward modeling is shown in Appendix B.

3.3. Keck/KPIC

We observed the HIP 55507 AB system with the upgraded Keck/NIRSPEC (Martin et al. 2018) using the KPIC fiber injection unit (FIU; Mawet et al. 2017; Delorme et al. 2021; Echeverri et al. 2022) on UT 2021 July 4 and 2023 May 2 (see Table 3). The FIU is located downstream of the Keck II adaptive optics system and is used to inject light from a selected target into one of the single-mode fibers connected to NIRSPEC. We obtained $R \sim 35,000$ spectra in the K band,

which is broken up into nine echelle orders from 1.94 to 2.49 μm . The observing strategy is similar to that of Wang et al. (2021), except we “nodded” between two fibers to enable background subtraction between adjacent frames. We also acquire short exposures of HIP 55507 A before observing the companion and spectra of a nearby A0 standard star (HIP 56147) at similar air mass.

We briefly summarize the KPIC data reduction procedure with the public Python pipeline.²⁶ For details, see Wang et al. (2021). First, we apply nod subtraction between adjacent frames as the spectral trace of each fiber lands on a different location in the detector. We also remove persistent bad pixels

²⁶ https://github.com/kpicteam/kpic_pipeline

identified from the background frames. Then, we use data from the telluric standard star to fit the trace of each column in the four fibers (two of which contain science data) and nine spectral orders, which give the position and standard deviation of the PSF in the spatial direction at each column. The trace positions and widths are additionally smoothed using a cubic spline to mitigate random noise.

For every frame, we extracted the 1D spectra in each column of each spectral order. To remove residual background light, we subtracted the median of pixels that are at least 5 pixels away from every pixel in each column. Finally, we used optimal extraction (Horne 1986) to sum the flux using weights defined by the 1D Gaussian line-spread function (LSF) profiles calculated from spectra of the telluric star.

For our analysis, we use three spectral orders from 2.29 to 2.49 μm , which contain strong absorption lines of CO and H₂O from the companion and CO from the primary star. These orders also have relatively few telluric absorption lines. Note that the three spectral orders have gaps in between them, so the KPIC data effectively cover a range of $\approx 0.13 \mu\text{m}$ after accounting for the gaps.

4. Basic Properties of HIP 55507 B

4.1. Orbit Fits with Relative RVs

The relative RV between HIP 55507 A and B can be directly measured from our KPIC data. From the two KPIC epochs, we extract two relative RV points (listed in Appendix C) from fitting the KPIC spectra of both HIP 55507 A and B (see Section 5).

In the Hipparcos-Gaia Catalog of Accelerations (Brandt 2021), HIP 55507 A shows a significant proper motion anomaly with an S/N of ≈ 28 in the Gaia epoch, with an amplitude that is consistent with being induced by HIP 55507 B. We perform orbit fits using RVs of HIP 55507 A from HIRES, relative astrometry from NIRC2 imaging, Gaia and Hipparcos absolute astrometry, and two relative RV points between HIP 55507 A and B from KPIC. We use the `orvara` package (Brandt et al. 2021) for these fits, which is able to jointly fit the aforementioned data. For the primary mass, we use a Gaussian prior of $0.67 \pm 0.04 M_{\odot}$, doubling the standard deviation of $0.02 M_{\odot}$ between literature mass measurements (Table 1). We use log-uniform or uniform priors on the other parameters following Brandt et al. (2021). We tested orbit fits where we further increase the width of the primary mass prior to $0.67 \pm 0.08 M_{\odot}$ (or 12% of the mass) and find that the resulting posterior for the companion mass shifts by $< 1\%$, while the uncertainties on all parameters are consistent to the $< 15\%$ level.

Our orbit and mass measurements are summarized in Table 4. We find a dynamical mass of $88.0^{+3.4}_{-3.2} M_{\text{Jup}}$ from this baseline fit. We run a second orbit fit that excluded the KPIC relative RVs to assess their effect on the results. We find that the addition of the two relative RV points from KPIC reduces the companion’s mass uncertainty by $\approx 60\%$ and shifts the median of the mass posterior to slightly higher values, as shown in Figure 2. The uncertainty on the orbital eccentricity also reduces by $\approx 50\%$ when including the relative RVs, and we find a moderate eccentricity of 0.40 ± 0.04 . In Figure 2, we visualize the effect of the relative RVs by plotting random draws from the posteriors of the relative RV (red) and no relative RV (blue) fits. While the overall orbital trend is

Table 4
Selected Parameters from Orbit Fit

Parameter	Value
$M (M_{\odot})$	0.675 ± 0.037
$m (M_{\text{Jup}})$	$88.0^{+3.4}_{-3.2}$
a (au)	$37.8^{+3.5}_{-2.7}$
Inclination (deg)	119.3 ± 0.7
Ascending node (deg)	219.9 ± 0.7
Period (yr)	266^{+44}_{-33}
Argument of periastron (deg)	$243.9^{+5.3}_{-5.8}$
Eccentricity	0.40 ± 0.04
Epoch of periastron (JD)	$2549330^{+16644}_{-12418}$

Note. A Gaussian prior of $0.67 \pm 0.04 M_{\odot}$ was imposed on the primary star mass.

constrained by the other data, the KPIC relative RVs help narrow down the spread in relative RV space, thereby reducing the companion mass uncertainty.

4.2. Bulk Properties and Evolutionary State

We place HIP 55507 B on a color–magnitude diagram (CMD) in Figure 3. As shown, HIP 55507 B is consistent with a late-M spectral type and located very close to Trappist-1 A (an M8.0 star; Gillon et al. 2016) on the CMD. Indeed, Trappist-1 A has an inferred mass of $93 \pm 6 M_{\text{Jup}}$ from model fitting (Grootel et al. 2018), very similar to the dynamical mass we measure for HIP 55507 B. Using relations in Dupuy & Liu (2012) and our measured absolute K_{MKO} of 9.63 ± 0.04 , we estimate a spectral type of $M7.5 \pm 0.5$ for HIP 55507 B.

From our spectral retrievals on the KPIC K-band spectra ($R \sim 35,000$) and K , L' , and M_s photometry, we estimate $\log(L_{\text{bol}}/L_{\odot}) = -3.29 \pm 0.02$ for HIP 55507 B (see details in Section 7).²⁷ In Figure 4, we place HIP 55507 B’s L_{bol} on isochrone tracks from Baraffe et al. (2015) and find that the companion falls between the 0.08 and 0.09 M_{\odot} isochrones. Therefore, the dynamical mass and L_{bol} for HIP 55507 B are consistent with the Baraffe et al. (2015) substellar model for an age of $\sim 1\text{--}2$ Gyr, suggesting that the companion has likely reached the hydrogen-burning main sequence.

5. Spectral Analysis Framework

In this section, we describe the framework to analyze KPIC spectroscopy of both HIP 55507 A and B. First, we describe the forward model for KPIC (Section 5.1), including the model we use to fit fringing modulations (Section 5.1.1). Then, we describe the PHOENIX-ACES grid model fits to HIP 55507 A spectra (Section 5.2). Lastly, we lay out the atmospheric retrieval setup (Section 5.3), which is applied to both HIP 55507 A and B to measure their molecular and/or isotopic abundances.

5.1. Forward Model of the KPIC Spectrum

Our forward model for KPIC spectra largely follows the framework in Xuan et al. (2022), with a few updates. In summary, we generate atmospheric templates with `petitRADTRANS` (Mollière et al. 2019, 2020). These templates are

²⁷ As a second estimate of L_{bol} , we use the empirical relation from Sanghi et al. (2023) between K_{MKO} and L_{bol} to obtain $\log(L_{\text{bol}}/L_{\odot}) = -3.21 \pm 0.08$, where the rms scatter of the empirical relation is folded into our luminosity uncertainty. This is consistent with our spectrally derived L_{bol} .

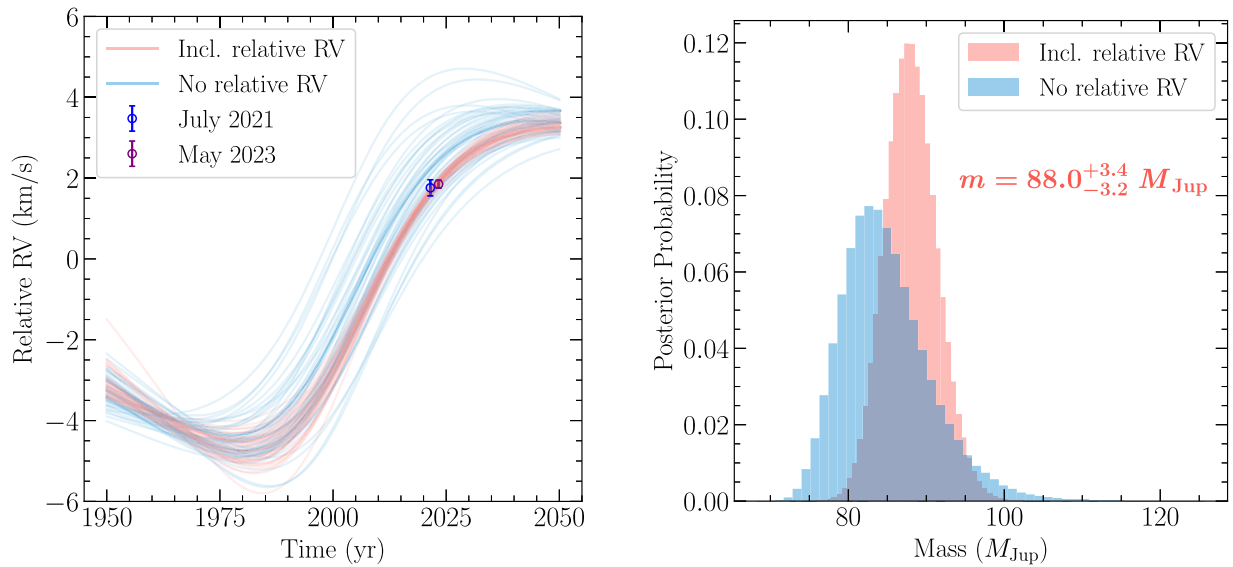


Figure 2. Left: model relative RV of the HIP 55507 AB system over time from random draws to the posterior distributions of the orbit fits. The red and blue curves are from the fit with and without the relative RVs, respectively. The data points show the observed relative RVs from KPIC. Right: the companion mass posteriors with (red) and without (blue) using the relative RVs, which show a reduction in the mass uncertainty and a slight shift of the median value when the relative RV is incorporated.

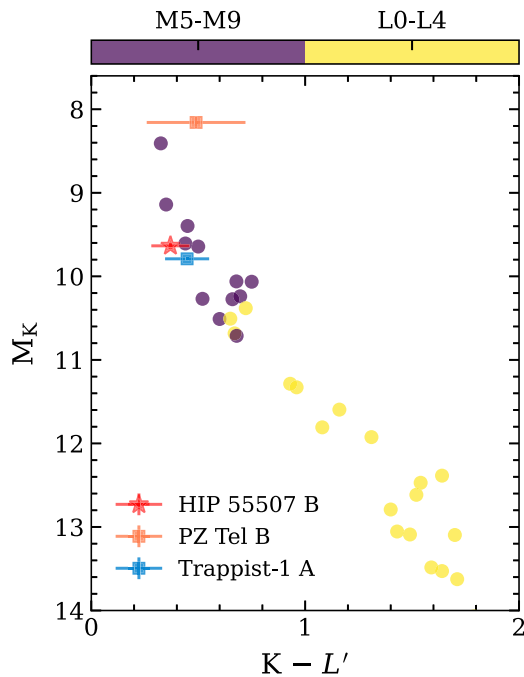


Figure 3. A CMD with M_K and $K - L'$. HIP 55507 B is shown as the red star, whereas purple and yellow points in the background are field brown dwarfs with late-M and early-L spectral types, respectively. We also label PZ Tel B, a late-M type substellar companion (Billier et al. 2010; Maire et al. 2016; Stolker et al. 2020), and Trappist-1 A (Cutri et al. 2003, 2021), both of which have properties similar to HIP 55507 B.

shifted in RV, and rotational broadening is performed using the open-source function from Carvalho & Johns-Krull (2023).²⁸

²⁸ We note that the commonly used `fastRotBroad` function from `PyAstronomy` (Czesla et al. 2019) is only valid for small wavelength arrays, and the question of how small depends on spectral resolution. At $R \sim 35,000$, our injection-recovery tests (Section 6) show `fastRotBroad` can lead to $v \sin i$ biases at the $\sim 10\%$ level for $v \sin i \sim 5 \text{ km s}^{-1}$. In contrast, the Carvalho & Johns-Krull (2023) method is accurate over arbitrarily large wavelength grids.

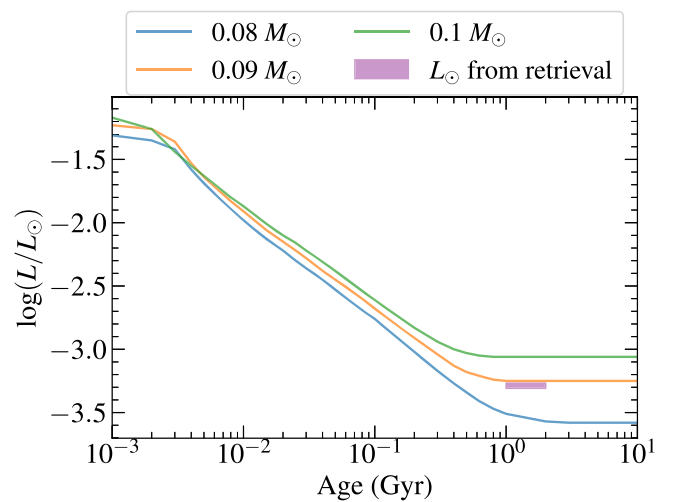


Figure 4. Isochrones from Baraffe et al. (2015) for three different masses. We show the measured L_{bol} for HIP 55507 B from spectral retrievals and the estimated age of 1–2 Gyr for the system as the purple shaded region. Both this region and the dynamical mass ($0.084 \pm 0.003 M_{\odot}$) lie in between the 0.08 and 0.09 M_{\odot} isochrones, suggesting that HIP 55507 B’s measured properties are consistent with the evolutionary model, and that it is likely on the hydrogen-burning main sequence.

Next, we convolve the RV-shifted and rotationally-broadened templates with the instrumental LSF, which we determine from the spectral trace widths in the spatial direction (Section 3.3). As noted by Wang et al. (2021), NIRSPEC was designed with a difference in focal lengths in the spatial and dispersion directions by a factor of 1.13 (Robichaud et al. 1998). Following Wang et al. (2021), we conservatively allow the LSF width to vary between 1.0 and 1.2 times the width measured in the spatial direction when generating the instrument-convolved companion templates. This uncertainty propagates to our $v \sin i$ uncertainty.

Next, the atmospheric template is multiplied by the telluric and instrumental response, which we determine from spectra of the standard star HIP 56147. For the primary star, HIP 55507 A, that

completes the forward model. For the companion, HIP 55507 B, the above procedures constitute a portion of its forward model. The other portion we need to consider for the companion is speckle contribution from the primary star, which we find to account for $\sim 1\%$ – 10% of the total flux in HIP 55507 B’s spectra given the relatively small separation of $\approx 0''.75$ – $0''.8$ between HIP 55507 A and B. To model the speckle contribution in the companion data, we use observations of HIP 55507 A taken immediately before the companion exposures.

Finally, we flux-normalize the companion and stellar models and multiply them by different flux scale factors, which are in units of counts as measured by NIRSPEC. After scaling, the companion and speckle models are added in the case of HIP 55507 B. To remove the smoothly varying continuum in the KPIC spectra, we apply high-pass filtering with a median filter of 100 pixels ($\sim 0.002 \mu\text{m}$) on the data and forward models for both HIP 55507 A and B. The choice of 100 pixels was found to be optimal for KPIC data from Xuan et al. (2022) for accurately retrieving molecular abundances in KPIC data. To summarize, the forward model for HIP 55507 B is

$$\text{FM}_B = \alpha_c T M_c + \alpha_s D_s, \quad (1)$$

where FM_B denotes the forward model for HIP 55507 B, α_c and α_s are the flux scales of the companion and speckle, T is the telluric and instrumental response, M_c is the companion template from `petitRADTRANS`, and D_s is the observed KPIC spectra of HIP 55507 A, which already has T factored in. In contrast, the forward model for HIP 55507 A is

$$\text{FM}_A = \alpha_A T M_A, \quad (2)$$

where α_A is the flux scale of the primary star in its on-axis observations, M_A is the primary star template from `petitRADTRANS`, and T is the same transmission function as above. The median filter is applied to both sides of these equations. In reality, we find additional modulation in the HIP 55507 AB data from fringing, which we also account for in our models.

5.1.1. Fringing Model for KPIC Data

KPIC data are affected by a time-varying fringing effect that produces quasiperiodic wiggles in the spectra that can imitate spectral absorption features (Finnerty et al. 2022). Given the high S/N of the HIP 55507 A and B spectra, we noticed that the dominant component in the residuals is due to fringing. We describe the details of our fringing model in Appendix D. Here, we simply point out that one optic in KPIC (a dichroic) causes the fringing signal to change between the HIP 55507 A spectra and the off-axis HIP 55507 B spectra. The characteristic fringe period induced by this dichroic is $\sim 4 \text{ \AA}$ at $2.3 \mu\text{m}$ (see Figure 5). We note that the fringe model effectively modifies the T component of Equations (1) and (2) with an additional transmission term and therefore applies to all our spectral fits for HIP 55507 A and B.

To incorporate fringing in our spectral fits, we adopt a three-step approach. First, we fit the spectra without the fringe model. The residuals from this first fit are characterized by fringing modulations. Second, we perform a least-squares optimization in the residuals of the first fit to find the best-fit fringing parameters that minimize the fringing signal. Third, in the final spectral fit, we fit the atmospheric parameters and fringe parameters jointly while adopting the best-fit fringe parameters

from the second step as initial guesses. The motivation for this is to avoid the excessively large and complex likelihood space from the fringe model while also incorporating uncertainties from the fringe model into our atmospheric parameters.

As described in Appendix D, our fringe model adds three parameters for each spectral order. In Figure 5, we plot the periodogram of the residuals with and without including the fringing model when fitting HIP 55507 A spectra. The power between ≈ 4 and 4.5 \AA is noticeably attenuated by the fringe model.

5.2. PHOENIX-ACES Model Fits to HIP 55507 A

To derive the primary star’s bulk properties, we first fit its KPIC spectra with the PHOENIX-ACES model (Husser et al. 2013), which here constitutes M_A in Equation (2). Specifically, we use two spectral orders spanning 2.29 – $2.41 \mu\text{m}$, with a gap in between. Our model grid assumes solar metallicity, and we vary the T_{eff} , $\log g$, RV , $v \sin i$, and stellar flux scale (α_A in Equation (2)). The parameters for the PHOENIX-ACES model fits are summarized in Table 6. We note that for HIP 55507 A, $v \sin i$ acts as a stand-in for the combined effects of rotational broadening and macroturbulence.²⁹ The results of the PHOENIX-ACES fits are presented in Appendix E. Next, we fit the HIP 55507 A spectra using a retrieval framework (see below).

5.3. Atmospheric Retrieval Setup

Here, we describe the atmospheric retrieval setup for HIP 55507 B and A to generate M_c and M_A in Equations (1) and (2), respectively. Retrievals allow us to measure the isotopologue abundances in both stars. Specifically, we set up radiative transfer routines with `petitRADTRANS` using the line-by-line opacity sampling method and down-sample the native $R = 10^6$ opacity tables by a factor of 3 to speed up the retrievals. In the following, we describe the opacities, chemistry, temperature profile, and cloud models used in the retrievals. The fitted parameters for HIP 55507 B are summarized in Table 5.

We note that compared to the retrieval analysis of HIP 55507 B, our retrievals for HIP 55507 A contain several simplifications, which we highlight throughout this section. Carrying out a retrieval with a free temperature profile and chemical abundances, as we do for HIP 55507 B, is not realistic at this stage for HIP 55507 A. Our K -band spectrum for this K6V star is dominated by CO lines with minor contributions from a few atomic lines. H_2O is mostly dissociated in the K6V star’s photosphere such that we cannot constrain the relative ratios of C and O. With more wavelength coverage (e.g., $H+K$ bands to probe OH, CO, and CN), a spectral synthesis approach could be a way to measure elemental abundances and C/O for HIP 55507 A, as achieved for a K7V dwarf by Hejazi et al. (2023).

5.3.1. Opacity Sources

We require high-temperature opacities for our stars. For HIP 55507 B, our preliminary retrievals show that there is a contribution to the emission spectrum from regimes with $T > 3000 \text{ K}$ (see Figure 6), which exceeds the 3000 K upper limit of default `petitRADTRANS` opacity tables for molecules

²⁹ The effects from macroturbulent broadening and rotation are similar and difficult to distinguish at low velocities. Microturbulent broadening is taken into account by the PHOENIX-ACES models, which adopt a microturbulent velocity of 0.48 km s^{-1} (Husser et al. 2013) for an atmosphere with properties similar to our K6V star ($T_{\text{eff}} = 4300 \text{ K}$, $\log g = 4.5$; see Table 1).

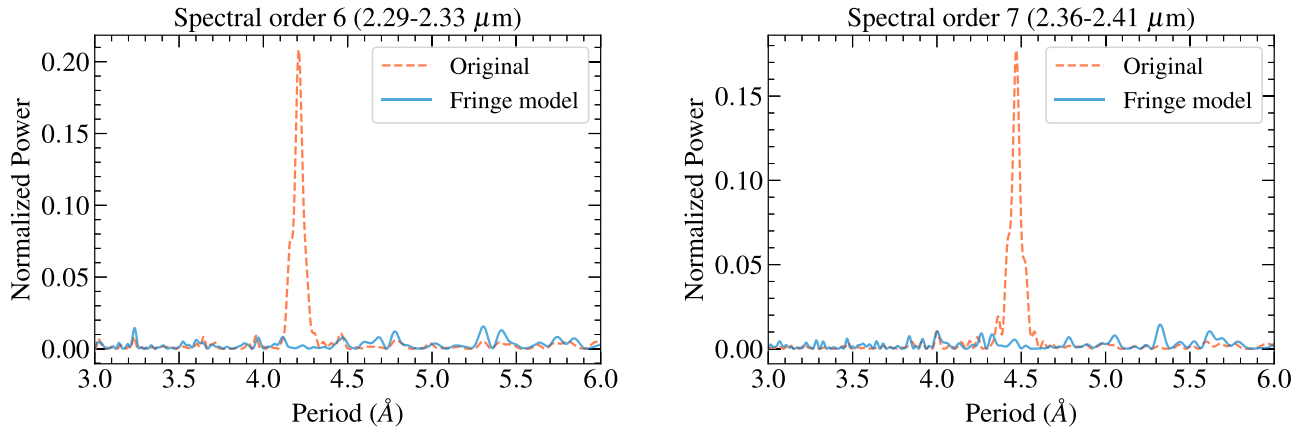


Figure 5. Lomb–Scargle periodograms of the residuals from fitting the KPIC spectra of HIP 55507 A. The blue and red periodograms are generated from the residuals of fits with and without the fringing model, respectively. The power between ≈ 4 and 4.5 Å, which is the characteristic frequency of fringing from the KPIC dichroic, is greatly diminished. The two panels are for different spectral orders.

Table 5
Fitted Parameters and Priors in HIP 55507 B Retrievals

Parameter	Prior	Parameter	Prior
Mass (M_{Jup})	$\mathcal{N}(88.0, 3.4)$	Radius (R_{Jup})	$\mathcal{U}(0.6, 2.5)$
T_{anchor} (K)	$\mathcal{U}(1900, 2700)$	RV (km s^{-1})	$\mathcal{U}(-30, 30)$
ΔT_1 (K)	$\mathcal{U}(400, 1000)$	$v \sin i$ (km s^{-1})	$\mathcal{U}(0, 30)$
ΔT_2 (K)	$\mathcal{U}(50, 700)$	C/O	$\mathcal{U}(0.1, 1.0)$
ΔT_3 (K)	$\mathcal{U}(50, 600)$	[C/H]	$\mathcal{U}(-1.5, 1.5)$
ΔT_4 (K)	$\mathcal{U}(50, 600)$	$\log(^{12}\text{CO}/^{13}\text{CO})$	$\mathcal{U}(0, 6)$
ΔT_5 (K)	$\mathcal{U}(50, 600)$	$\log(\text{H}_2^{16}\text{O}/\text{H}_2^{18}\text{O})$	$\mathcal{U}(0, 6)$
ΔT_6 (K)	$\mathcal{U}(50, 600)$	$\log(\text{C}^{16}\text{O}/\text{C}^{18}\text{O})$	$\mathcal{U}(0, 6)$
ΔT_7 (K)	$\mathcal{U}(50, 600)$	$\log(\text{gray opacity}/\text{cm}^2 \text{g}^{-1})^a$	$\mathcal{U}(-6, 6)$
f_{sed}^b	$\mathcal{U}(0, 10)$	$\log(K_{\text{zz}}/\text{cm}^2 \text{s}^{-1})^b$	$\mathcal{U}(5, 13)$
σ_g^b	$\mathcal{U}(1.05, 3)$	$\log(\bar{X}_{\text{Al}_2\text{O}_3})^b$	$\mathcal{U}(-2.3, 1)$
Fringe and Other Parameters			
Optical path length, d (mm)	$\mathcal{U}(4, 5)$	Comp. flux, α_c (counts)	$\mathcal{U}(0, 300)$
Fractional amplitude, F	$\mathcal{U}(10^{-6}, 1)$	Speckle flux, α_s (counts)	$\mathcal{U}(0, 200)$
Dichroic temperature, T_d (K)	$\mathcal{U}(150, 330)$	Error multiple ^c	$\mathcal{U}(1, 5)$

Notes. \mathcal{U} stands for a uniform distribution, with two numbers representing the lower and upper boundaries. \mathcal{N} stands for a Gaussian distribution, with numbers representing the median and standard deviation. The fringe parameters d , F , and T_d are described in Appendix D.

^a Parameter for the gray cloud model (constant gray opacity).

^b Parameters for the EddySed cloud model. $\bar{X}_{\text{Al}_2\text{O}_3}$ is the scaling factor for the cloud mass fraction, so that $\log(\bar{X}_{\text{Al}_2\text{O}_3}) = 0$ refers to a fraction equal to the equilibrium mass fraction. Together, f_{sed} , K_{zz} , and σ_g set the cloud mass fraction as a function of pressure and the cloud particle size distribution (Mollière et al. 2020).

^c The error multiple term is fitted for KPIC data to account for any underestimation in the uncertainties.

(Mollière et al. 2019). Therefore, whenever possible, we update our opacity tables to go to $T_{\text{max}} = 4500$ K or higher using the DACE opacity database generated with the HELIOS-K opacity calculator (Grimm & Heng 2015; Grimm et al. 2021).³⁰ In particular, we upgrade the line opacities of H_2^{16}O (Polyansky et al. 2018), OH (Brooke et al. 2016), FeH (Dulick et al. 2003; Bernath 2020), TiO (McKemmish et al. 2019), AlH (Yurchenko et al. 2018), and VO (McKemmish et al. 2016) to reach 4500 K. For H_2^{18}O , we adopt the line list from Polyansky et al. (2017), which is valid up to 3000 K. For H_2S , we use the line list from Azzam et al. (2016), valid up to 2000 K. Finally, we include the atomic line species Na, K, Mg, Ca, Ti, Fe, and Al (Kurucz 2011).

For HIP 55507 A, the photosphere is at even higher temperatures, but the K-band spectrum of this star is dominated

by mostly CO and the aforementioned atomic lines. Therefore, we only include these opacities for the HIP 55507 A retrievals. We generate opacities for C^{16}O , ^{13}CO , and C^{18}O that are valid up to 9000 K from Rothman et al. (2010).

For the continuum opacities in both stars, we include the collision-induced absorption from H_2 – H_2 and H_2 –He, as well as the H- bound-free and free-free opacity.

5.3.2. Chemistry and Isotopologue Ratios

The default chemical equilibrium grid in `petitRADTRANS` does not save the abundances of all the species we include as opacity sources. Therefore, we generate a custom chemical equilibrium grid using `easyCHEM`,³¹ which is the same code used by Mollière et al. (2020). We validated our new grid

³⁰ <https://dace.unige.ch/opacityDatabase/>

³¹ <https://easychem.readthedocs.io/en/latest/content/installation.html>

against the `petitRADTRANS` chemical grid for overlapping species and find excellent agreement (fractional differences of $<1\%$). The abundances of species are set by two parameters in our grid, the carbon abundance $[C/H]$ and the carbon-to-oxygen ratio C/O , which together determine the oxygen abundance. We are only sensitive to the abundances of C and O in this work; therefore, we assume that the other metals scale with C. Our grid goes up to 8000 K, more than hot enough for the K6V primary star. For the solar elemental abundances, we adopt Asplund et al. (2009).

In our retrievals, the abundances of the main isotopologues are obtained from interpolating the chemical equilibrium grid for each value of C/O and $[C/H]$. Then, for each minor isotopologue included, we fit for an isotopologue ratio parameter akin to Zhang et al. (2021a). In our baseline retrievals, we fit for three ratios: $^{12}C^{16}O/^{13}C^{16}O$, $^{12}C^{16}O/^{12}C^{18}O$, and $H_2^{16}O/H_2^{18}O$. This allows us to explore whether the $^{16}O/^{18}O$ ratio differs between CO and H_2O , which may arise from isotopic fractionation processes such as self-shielding of CO and UV shielding of H_2O (Calahan et al. 2022). In addition, fitting two ratios allows us to examine whether the data show evidence for $H_2^{18}O$, $^{12}C^{18}O$, or both.

5.3.3. Temperature Structure

For HIP 55507 B, we adopt a modified version of the pressure–temperature (P – T) profile from Piette & Madhusudhan (2020). Our profile is parameterized by seven $\Delta T/\Delta P$ values between eight pressure points and the temperature at one of these pressures. Instead of having the pressure points equally spaced in log pressure, we preferentially concentrate pressure points around the peak of the weighted emission contribution, as this is where the data are most informative. The selected pressure points are labeled in Figure 6, and the modeled pressure extent is between $\log(\text{bar}) = -4.0$ and 1.4. For the radiative transfer, the eight P – T points from our profile are interpolated onto a finer grid of 100 P – T points using a monotonic cubic interpolation as recommended by Piette & Madhusudhan (2020). Unlike Piette & Madhusudhan (2020), we do not apply smoothing to our profiles, as smoothing has been shown to bias retrieval results (Rowland et al. 2023).

For HIP 55507 A, we fix its P – T profile to a Phoenix P – T profile (Husser et al. 2013) matching the properties of the star ($T_{\text{eff}} = 4300$ K and $\log g = 4.5$) for simplicity.

5.3.4. Clouds

Clouds are expected to play a minimal role for late-M objects like HIP 55507 B and no role for a K6V star like HIP 55507 A, as temperatures are too hot for cloud condensates to remain stable. For completeness in our HIP 55507 B retrievals, we consider both clear and cloudy models to explore the sensitivity of our retrieved abundances to assumed cloud properties. For the cloudy models, we use a gray cloud model, where a constant opacity is added to the atmosphere, and the EddySed model (Ackerman & Marley 2001) as implemented in `petitRADTRANS` (Mollière et al. 2020). We used Al_2O_3 clouds in the EddySed model, as Al_2O_3 is expected to be more important at higher T_{eff} (Wakeford & Sing 2015).

5.3.5. Summary of Retrieval Setup for Both Stars

As noted earlier, we make simplifications in retrieving the spectra of HIP 55507 A. To summarize the retrieval setup for

A, we (1) adopt priors on C/O and $[C/H]$ for HIP 55507 A using measured values from HIP 55507 B, (2) fix the P – T profile to a Phoenix P – T profile (Husser et al. 2013), and (3) allow the stellar mass and radius to vary within 1σ intervals given in Table 1.

In contrast, we freely fit for all these parameters in the HIP 55507 B retrievals, with the exception of mass. For the companion’s mass, we adopt a dynamical mass prior determined from Section 4. The fitted parameters and adopted priors in HIP 55507 B and A retrievals are listed in Tables 5 and 6, respectively.

5.3.6. Jointly Fitting Photometry for HIP 55507 B

For HIP 55507 B, we jointly fit the KPIC high-resolution spectra with the K , L' , and M_s photometric points in Table 2 to better constrain the bulk properties of the companion. The apparent magnitudes were converted into flux density units by computing the zero-point for each photometric filter using the `species` package (Stolker et al. 2020). For the photometry model, we use the correlated- k opacities in `petitRADTRANS` (rebinned to $R = 50$). The photometry model does not add any new parameters, as it is fully described by the atmospheric parameters introduced earlier. In joint KPIC+photometry retrievals, we add the log likelihoods from the photometry and KPIC components.

5.3.7. Model Fitting with Nested Sampling

We use nested sampling as implemented by `dynesty` (Speagle 2020) to find the posterior distributions for all model parameters listed in Table 5 for HIP 55507 B and Table 6 for HIP 55507 A. We use 600 live points and adopt the stopping criterion that the estimated contribution of the remaining prior volume to the total evidence is less than 1%. We confirmed that increasing the number of live points to 1000 does not meaningfully change the posteriors of our retrieved parameters.

6. Injection-recovery Tests

To validate our retrieval framework, we perform a series of injection-recovery retrievals on simulated data for HIP 55507 B. We inject model spectrum from `petitRADTRANS` in the extracted spectrum of a non-illuminated fiber. Such a fiber still measures the thermal background of the instrument and serves as a realistic “noise spectrum,” since thermal noise is the dominant source of noise for our data. Specifically, we use the extracted fiber 4 trace at the time of observations. We took the fiber 4 trace on exposures where HIP 55507 B was aligned to fiber 2, at which time fiber 4 was located $\sim 2''$ away from the companion and $\sim 2''.5$ away from HIP 55507 A. Examination of the extracted spectra from fiber 4 shows that there is negligible leaked light; the median of the flux is ≈ 0 counts. We multiply the companion model by the telluric response function (T) for fiber 4, add a speckle flux contribution using the primary star spectra, and high-pass filter the simulated data in the same way as for the real data.

For the input companion model, we use a P – T profile from the SPHINX model grid (Iyer et al. 2023) with $T_{\text{eff}} = 2500$ K, $\log g = 5.25$, solar metallicity, and $C/O = 0.7$. We set the mass ($87 M_{\text{Jup}}$) and radius ($1.1 R_{\text{Jup}}$) of our injected companion to be consistent with this $\log g$ and the chemical abundances to $C/O = 0.7$ and $[C/H] = 0$, consistent with that assumed in the

P - T profile. To achieve a similar S/N as the real data, we inject similar companion and speckle flux values as the data. We carry out two injections at different RV shifts (-10 and 10 km s^{-1}) to sample various parts of the background trace. In addition to simulating a KPIC model, we also simulate three photometry points using the same input values. The parameters of the simulated models are given in Table 7.

In our simulated model, we inject $^{12}\text{CO}/^{13}\text{CO} = 100$ ($\log(^{12}\text{CO}/^{13}\text{CO}) = 2.0$) and $\text{H}_2^{16}\text{O}/\text{H}_2^{18}\text{O} = 200$ ($\log(\text{H}_2^{16}\text{O}/\text{H}_2^{18}\text{O}) \approx 2.301$), similar to what we find in the real data. Since we do not detect $\text{C}^{16}\text{O}/\text{C}^{18}\text{O}$ in the data, we inject a lower value of $\text{C}^{16}\text{O}/\text{C}^{18}\text{O} = 600$ ($\log(\text{C}^{16}\text{O}/\text{C}^{18}\text{O}) \approx 2.778$) to see whether this can be recovered in our tests. Note that our isotopologue ratios are fitted in log scale in the retrieval.

As shown in Table 7, $\log(^{12}\text{CO}/^{13}\text{CO})$ and $\log(\text{H}_2^{16}\text{O}/\text{H}_2^{18}\text{O})$ are recovered, though systematic offsets of 0.05 – 0.1 dex can be present in the retrieved $\log(^{12}\text{CO}/^{13}\text{CO})$. On the other hand, the systematic bias is only ~ 0.03 dex for $\log(\text{H}_2^{16}\text{O}/\text{H}_2^{18}\text{O})$. To be conservative, we adopt 0.1 dex as the systematic error for both of these isotopologue ratios in our retrievals of the real data. The $\log(\text{C}^{16}\text{O}/\text{C}^{18}\text{O})$ posterior is not well bounded, though the 3σ lower limit for $\log(\text{C}^{16}\text{O}/\text{C}^{18}\text{O})$ does contain the injected value. Further tests show that we cannot reliably retrieve values of $\text{C}^{16}\text{O}/\text{C}^{18}\text{O} = 200$ – 300 , suggesting it is harder to detect C^{18}O compared to H_2^{18}O with our KPIC spectra. From examining the C^{18}O opacities, we find that this is may be due to the fact that many C^{18}O lines overlap in wavelength with ^{13}CO lines, thereby masking the weaker signal from C^{18}O .

From the injection-recovery tests, we find that C/O and [C/H] are well recovered, with only ~ 0.01 deviations in C/O between the injected and recovered values and < 0.02 dex deviations in the [C/H] values. We attribute the slight offsets between the injected and retrieved values to random noise in the background trace.

As mentioned in Section 5.3, the choice of rotational broadening kernel can have an impact on the retrieved $v \sin i$. Even when using the direct integration method from Carvalho & Johns-Krull (2023), we note that the retrieved $v \sin i$ can still be biased by the down-sampling factor for the line-by-line opacities. At the KPIC resolution of $R \sim 35,000$ and for a $v \sin i$ of 5.0 km s^{-1} (technically below our resolution limit of $\sim 7.5 \text{ km s}^{-1}$), we find that down-sampling the native $R = 10^6$ opacities by a factor of 3 or less allows us to accurately recover the input $v \sin i$ of 5.0 km s^{-1} .

7. Retrieval Results

7.1. HIP 55507 B

We run three sets of retrievals for HIP 55507 B: two sets for the 2021 and 2023 KPIC data sets separately and one set that combines the 2021 and 2023 KPIC data. By default, we include the K , L' , and M_s photometric data in the retrievals, but we also tested fits where we excluded the photometry. Retrieved parameters from each set of retrievals are presented in Table 8, and the baseline retrieval (2021+2023+photometry) is in bold. We plot the KPIC spectra and best-fit models in Figure 7, while the photometry fit is shown in Figure 8. The joint posterior distributions of a few parameters from the baseline retrieval are shown in Figure 9.

7.1.1. P - T Profile and Clouds

The P - T profile from the baseline retrieval (clear model) is shown in Figure 6. The cloudy models give almost identical P - T shapes as the clear model. We find that the lower atmosphere is fairly consistent with the self-consistent SPHINX models from Iyer et al. (2023), but the upper atmosphere is hotter and more isothermal. This could be due to a trade-off between clouds and an isothermal P - T profile, which is seen in most retrieval studies (e.g., Burningham et al. 2017; Xuan et al. 2022; Brown-Sevilla et al. 2023; Whiteford et al. 2023). As demonstrated by Xuan et al. (2022), narrowband high-resolution spectra can be largely insensitive to clouds but still sensitive to gas-phase molecular abundances. To check if the isothermal upper P - T profile affects our results, we ran a retrieval for HIP 55507 B with the P - T profile fixed to the $T_{\text{eff}} = 2400 \text{ K}$, $\log g = 5.25$ SPHINX profile in Figure 6. The resulting posteriors from this retrieval are consistent with those from our baseline retrieval within 1σ , so we conclude that the isothermal upper atmosphere is not biasing our results.

For the 2023 KPIC data set, we tested three cloud models: clear, gray opacity, and EddySed with Al_2O_3 . To assess whether clouds are preferred by the data, we use the Bayesian evidence from each retrieval to calculate the Bayes factor B , which assesses the relative probability of an alternative model M_2 compared to M_1 . Here, we take the clear model to be M_1 . The data slightly prefer the gray opacity and EddySed models over the clear model, with $\ln(B) = 2.5$ and 2.3 , respectively, which correspond to $\sim 2.6\sigma$ preferences for the cloudy models using the Trotta (2008) scale. However, the cloud parameters are largely unconstrained, with a 3σ upper limit of $0.009 \text{ cm}^2 \text{ g}^{-1}$ for the gray opacity. The retrieved abundances are also identical between the cloudy and clear models (see Table 8), so we adopt the clear model as the baseline model.

7.1.2. Isotopologue Abundances of ^{13}CO and H_2^{18}O

In the KPIC data set from 2023, we strongly detect ^{13}CO and tentatively detect H_2^{18}O in the atmosphere of HIP 55507 B, with $\log(^{12}\text{CO}/^{13}\text{CO}) = 2.03 \pm 0.05$ and $\log(\text{H}_2^{16}\text{O}/\text{H}_2^{18}\text{O}) = 2.22 \pm 0.15$. The 2021 epoch gives $\log(^{12}\text{CO}/^{13}\text{CO}) = 1.80 \pm 0.08$, which is 0.23 dex or $\approx 2.4\sigma$ lower than the 2023 value. $\text{H}_2^{16}\text{O}/\text{H}_2^{18}\text{O}$ is unconstrained from the 2021 epoch due to its lower S/N. The discrepancy in $\log(^{12}\text{CO}/^{13}\text{CO})$ between data sets is somewhat higher than the 0.05 – 0.1 dex systematic bias we identify in our injection-recovery tests. In our reported values, which are based on a joint fit to both 2021 and 2023 data sets, we add a 0.1 dex systematic error in quadrature to the measurement errors. In summary, we report $^{12}\text{CO}/^{13}\text{CO} = 98_{-22}^{+28}$ and $\text{H}_2^{16}\text{O}/\text{H}_2^{18}\text{O} = 240_{-80}^{+145}$ for HIP 55507 B. $\text{C}^{16}\text{O}/\text{C}^{18}\text{O}$ is unconstrained, with a formal 3σ lower limit of ≈ 440 . However, as discussed in Section 6, we often cannot recover $\text{C}^{16}\text{O}/\text{C}^{18}\text{O}$ values of 200 – 300 from injection-recovery tests, so the true $\text{C}^{16}\text{O}/\text{C}^{18}\text{O}$ value could in fact be lower than 440 and consistent with our $\text{H}_2^{16}\text{O}/\text{H}_2^{18}\text{O}$ value.

To assess whether the ^{13}CO and H_2^{18}O isotopologues are needed to fit the data or whether we can adjust other parameters to improve the fits, we perform two retrievals with one of these isotopologues removed in each. These constitute the “reduced models.” We then calculate the Bayes factor between these

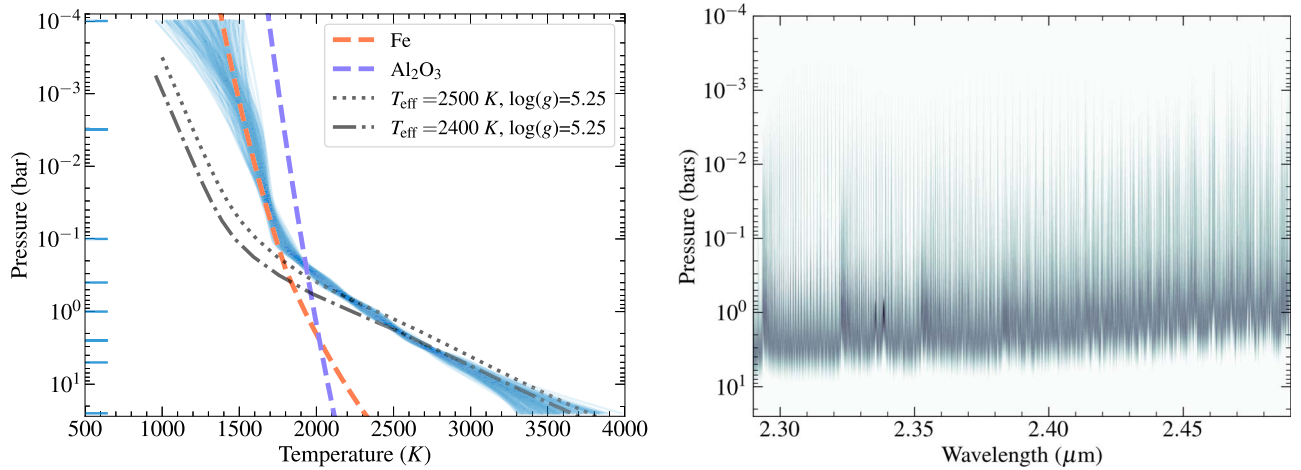


Figure 6. Left: random draws from the posterior of the retrieved P – T profiles from the baseline retrieval (blue). The gray lines show SPHINX models (Iyer et al. 2023) with similar bulk properties as HIP 55507 B. The condensation curves for Fe and Al_2O_3 clouds are plotted in colored dashed lines. The horizontal ticks on the y-axis are pressure points between which we fit ΔT values in our P – T parameterization. Right: the emission contribution function of the best-fit baseline model. There is nonzero contribution at ~ 5 bars, where the temperature profile (left panel) exceeds 3000 K.

Table 6
Fitted Parameters and Priors in HIP 55507 A Retrieval and PHOENIX-ACES Fit

Parameter (Retrieval)	Prior	Parameter (PHOENIX-ACES)	Prior
Mass (M_\odot)	$\mathcal{U}(0.63, 0.71)$	T_{eff} (K)	$\mathcal{U}(3000, 5500)$
Radius (R_\odot)	$\mathcal{U}(0.64, 0.72)$	$\log g$ (dex)	$\mathcal{U}(3.5, 5.5)$
$v \sin i$ (km s^{-1})	$\mathcal{U}(0, 30)$	$v \sin i$ (km s^{-1})	$\mathcal{U}(0, 30)$
RV (km s^{-1})	$\mathcal{U}(-30, 30)$	RV (km s^{-1})	$\mathcal{U}(-30, 30)$
C/O	$\mathcal{N}(B_\mu, B_\sigma)$		
[C/H]	$\mathcal{N}(B_\mu, B_\sigma)$		
$\log(^{12}\text{CO}/^{13}\text{CO})$	$\mathcal{U}(0, 6)$		
$\log(\text{C}^{16}\text{O}/\text{C}^{18}\text{O})$	$\mathcal{U}(0, 6)$		
Fringe and Other Parameters			
Optical path length, d (mm)	$\mathcal{U}(4, 5)$	Star flux, α_A (counts)	$\mathcal{U}(0, 10000)$
Fractional amplitude, F	$\mathcal{U}(10^{-6}, 1)$	Error multiple	$\mathcal{U}(1, 5)$
Dichroic temperature, T_d (K)	$\mathcal{U}(150, 330)$		

Note. Symbols for priors are the same as in Table 5. The parameters for the HIP 55507 A retrieval and PHOENIX-ACES fits are in the left and right columns, respectively. “Fringe and other parameters” are common to both. For C/O and [C/H], B_μ and B_σ represent the median and 1σ interval measured for the companion, HIP 55507 B, which are used as Gaussian priors in the HIP 55507 A retrieval.

reduced models and the full model with all isotopologues included, which are tabulated in Table 8. The $\ln(B)$ values correspond to a 7.8σ detection of ^{13}CO and 3.7σ detection of H_2^{18}O .

We can obtain a complementary perspective on the robustness of these detections using the cross-correlation method, following the approach in Zhang et al. (2021b) and Xuan et al. (2022). The goal of this analysis is to assess whether the full models prefer ^{13}CO and H_2^{18}O independent of

the Bayes factor calculation from our retrievals. To compute the cross-correlation function (CCF), we follow the framework from Ruffio et al. (2019), so the y-axis of our CCFs is the estimated flux level (in counts) of the isotopologue signal from a least-squares minimization.

First, we compute the CCF between a ^{13}CO -only model and the (data–model without ^{13}CO). The latter is equivalent to the residuals of the reduced model and will contain residual ^{13}CO lines if the data contain ^{13}CO . Then, we compute the CCF between the ^{13}CO -only model and the (data–model with ^{13}CO). This second CCF should not show a detection, as ^{13}CO is already fitted for in the model with ^{13}CO (i.e., the full model). We generate the isotopologue-only models by manually zeroing the opacities of all other line species except the isotopologue when computing the full model. The same process is repeated for H_2^{18}O , whose CCFs are shown in the right panel of Figure 10.

We find that the ^{13}CO signal is cleaner compared to the H_2^{18}O signal, as the CCF for H_2^{18}O shows stronger residual structure in the wings, although there is a peak around 0 km s^{-1} (companion’s rest frame) consistent with a real signal. However, because the remaining systematics are on a scale similar to that of the peak, we consider the H_2^{18}O detection to be tentative in these data. It is possible that this detection is produced by remnant fringing features that our fringe model did not perfectly remove and/or residual telluric features, which are especially strong in the 2.45 – $2.49 \mu\text{m}$ wavelength region where the H_2^{18}O lines are strongest. A future upgrade to KPIC should greatly reduce the fringing from the dichroics, allowing us to revisit H_2^{18}O in HIP 55507 B’s atmosphere with more confidence.

7.1.3. C/O and Atmospheric Metallicity

We retrieve $\text{C/O} = 0.68 \pm 0.01$, $[\text{C}/\text{H}] = 0.26 \pm 0.04$ for the 2023 epoch and $\text{C/O} = 0.64 \pm 0.01$, $[\text{C}/\text{H}] = 0.14 \pm 0.05$ for the 2021 epoch. These values are broadly consistent, with a $\sim 6\%$ difference in C/O and 0.12 dex difference in [C/H]. Notably, the $\sim 6\%$ difference in C/O between the two epochs is lower than the $\sim 15\%$ – 20% error estimated by Xuan et al. (2022) and Wang et al. (2022) for benchmark brown dwarf companions, where it was

Table 7
Input and Retrieved Parameters from Injection-recovery Tests

Parameter	RV (km s ⁻¹)	$v \sin i$ (km s ⁻¹)	C/O	[C/H]	log(¹² CO/ ¹³ CO)	log(H ₂ ¹⁶ O/H ₂ ¹⁸ O)	log(C ¹⁶ O/C ¹⁸ O)
Input values	10.0; -10.0	5.00	0.70	0.0	2.00	2.30	2.78
RV = 10 km s ⁻¹	9.96 ± 0.03	5.02 ± 0.09	0.706 ± 0.005	0.02 ± 0.03	2.05 ± 0.04	2.27 ± 0.05	...
RV = -10 km s ⁻¹	-10.05 ± 0.02	4.99 ± 0.09	0.693 ± 0.005	0.01 ± 0.03	1.90 ± 0.03	2.33 ^{+0.14} _{-0.11}	...

Note. The injections were performed on a non-illuminated KPIC fiber to sample realistic thermal noise properties. We place a Gaussian prior on the mass and so do not report this value.

Table 8
Spectral Retrievals and Results

Data/Observing Date	Isotopologues Included	C/O	[C/H]	¹² CO/ ¹³ CO	H ₂ ¹⁶ O/H ₂ ¹⁸ O	Radius (R_{Jup})	T_{eff} (K)	ln(B)
2023/05/02								
KPIC + Phot.	¹³ CO, H ₂ ¹⁸ O, C ¹⁸ O	0.68 ± 0.01	0.26 ± 0.04	106 ⁺¹⁴ ₋₁₁	165 ⁺⁶⁸ ₋₄₄	1.32 ± 0.02	2367 ± 20	0
KPIC + Phot.	H ₂ ¹⁸ O, C ¹⁸ O	0.68 ± 0.01	0.26 ± 0.04	...	150 ⁺⁸⁷ ₋₃₈	1.32 ± 0.02	2355 ± 20	-28.0
KPIC + Phot.	¹³ CO, C ¹⁸ O	0.68 ± 0.01	0.25 ± 0.05	103 ⁺¹² ₋₉	...	1.32 ± 0.02	2372 ± 20	-4.9
KPIC + Phot. (gray)	¹³ CO, H ₂ ¹⁸ O, C ¹⁸ O	0.68 ± 0.01	0.25 ± 0.04	106 ⁺¹³ ₋₁₁	163 ⁺⁶⁷ ₋₄₂	1.32 ± 0.02	2366 ± 20	2.5
KPIC + Phot. (Al ₂ O ₃)	¹³ CO, H ₂ ¹⁸ O, C ¹⁸ O	0.68 ± 0.01	0.25 ± 0.05	103 ⁺¹³ ₋₉	167 ⁺⁷² ₋₄₆	1.32 ± 0.02	2368 ± 20	2.3
KPIC	¹³ CO, H ₂ ¹⁸ O, C ¹⁸ O	0.69 ± 0.01	0.00 ± 0.12	114 ⁺¹⁵ ₋₁₂	172 ⁺⁶³ ₋₄₃	1.92 ± 0.27	2348 ± 20	...
2021/07/04								
KPIC + Phot.	¹³ CO, H ₂ ¹⁸ O, C ¹⁸ O	0.64 ± 0.01	0.14 ± 0.05	63 ⁺¹³ ₋₈	>120 (3 σ)	1.35 ± 0.02	2343 ± 25	0
KPIC + Phot.	H ₂ ¹⁸ O, C ¹⁸ O	0.64 ± 0.01	0.12 ± 0.05	...	>96 (3 σ)	1.35 ± 0.02	2351 ± 25	-14.8
2021/07/04 + 2023/05/02								
Adopted: KPIC + Phot.	¹³ CO, H ₂ ¹⁸ O, C ¹⁸ O	0.67 ± 0.04	0.24 ± 0.13	98 ⁺²⁸ ₋₂₂	240 ⁺¹⁴⁵ ₋₈₀	1.33 ± 0.02	2350 ± 50	...

Note. A few atmospheric parameters and their central 68% credible interval with equal probability above and below the median are listed. These values only account for statistical error. In the final row, we list the adopted values accounting for systematic errors from the retrieval. The rightmost column lists the log Bayes factor ln(B) for each retrieval. We compute ln(B) with respect to the baseline model for each data set, i.e., the models with ln(B) = 0. Unless specified in parentheses, we use a clear model. “Gray” refers to the gray opacity cloud model, and “Al₂O₃” refers to the EddySed model with Al₂O₃ clouds.

assumed that the brown dwarf companions have the same compositions as their host stars.

We adopt a systematic error of 0.04 in C/O and 0.12 dex in [C/H] for our baseline retrieval and report [C/H] = 0.24 ± 0.13, [O/H] = 0.15 ± 0.13, and C/O = 0.67 ± 0.04 for HIP 55507 B. The primary star HIP 55507 A has [Fe/H] = -0.02 ± 0.09 from Keck/HIRES spectra in the optical (Table 1), consistent with a solar metallicity. If we assume [Fe/H] = [C/H] for the primary star, this implies that the [C/H] between HIP 55507 A and B are consistent to within 1.6 σ .

7.1.4. Effective Temperature, Luminosity, and Radius

The addition of the photometry data in the K , L' , and M_s bands helps constrain the bulk parameters of HIP 55507 B. For example, when we omit the photometry for the 2023 May retrieval, the retrieved radius is $R = 1.92 \pm 0.27 R_{\text{Jup}}$, while retrievals with the photometry yield $R = 1.32 \pm 0.02 R_{\text{Jup}}$ (Table 8). We integrate the model spectra with parameters drawn from the posteriors of our baseline retrieval to compute $\log(L_{\text{bol}}/L_{\odot}) = -3.29 \pm 0.02$ and $T_{\text{eff}} = 2350 \pm 50$ K. While the statistical uncertainties on these parameters are small, we note that the model uncertainties are likely larger, since the flux information is derived from three photometric points covering a small portion of the L_{bol} budget.

Given measurements of the dynamical mass and L_{bol} , we can compare the spectrally inferred radius and T_{eff} to the predictions

from evolutionary models. To do so, we interpolate the AMES-COND, AMES-Dusty, and BHAC15 models (Allard et al. 2001; Baraffe et al. 2015) with Gaussian distributions of $m = 88.0 \pm 3.4 M_{\text{Jup}}$ and $\log(L_{\text{bol}}/L_{\odot}) = -3.29 \pm 0.02$. We find that the evolutionary models favor $R \approx 1.08 \pm 0.02 R_{\text{Jup}}$ and $T_{\text{eff}} = 2530 \pm 80$ K, i.e., a smaller radius and larger T_{eff} than the spectral retrievals. A similar radius- T_{eff} degeneracy has been noted by several retrieval studies, although the discrepancy is usually in the opposite direction for colder brown dwarfs, with retrievals finding a smaller radius than evolutionary models (e.g., Gonzales et al. 2022; Lueber et al. 2022; Hood et al. 2023). Sanghi et al. (2023) compared radii inferred by evolutionary and atmospheric models for a large sample of brown dwarfs and found significant discrepancies in T_{eff} and radius for late-M/early-L spectral types in both directions, which highlights ongoing challenges in measuring bulk properties from substellar atmospheric models and retrievals (see also Dupuy et al. 2010 for late-M dwarfs).

7.1.5. Projected Rotation Rate

We measure a relatively slow $v \sin i = 5.4 \pm 0.2$ km s⁻¹ for HIP 55507 B, which is below the KPIC resolution limit of ~ 7.5 km s⁻¹ at $R \sim 35,000$. The high S/N of the data allows us to tightly constrain $v \sin i$ values below the resolution limit, as we demonstrated using injection-recovery tests (Table 7).

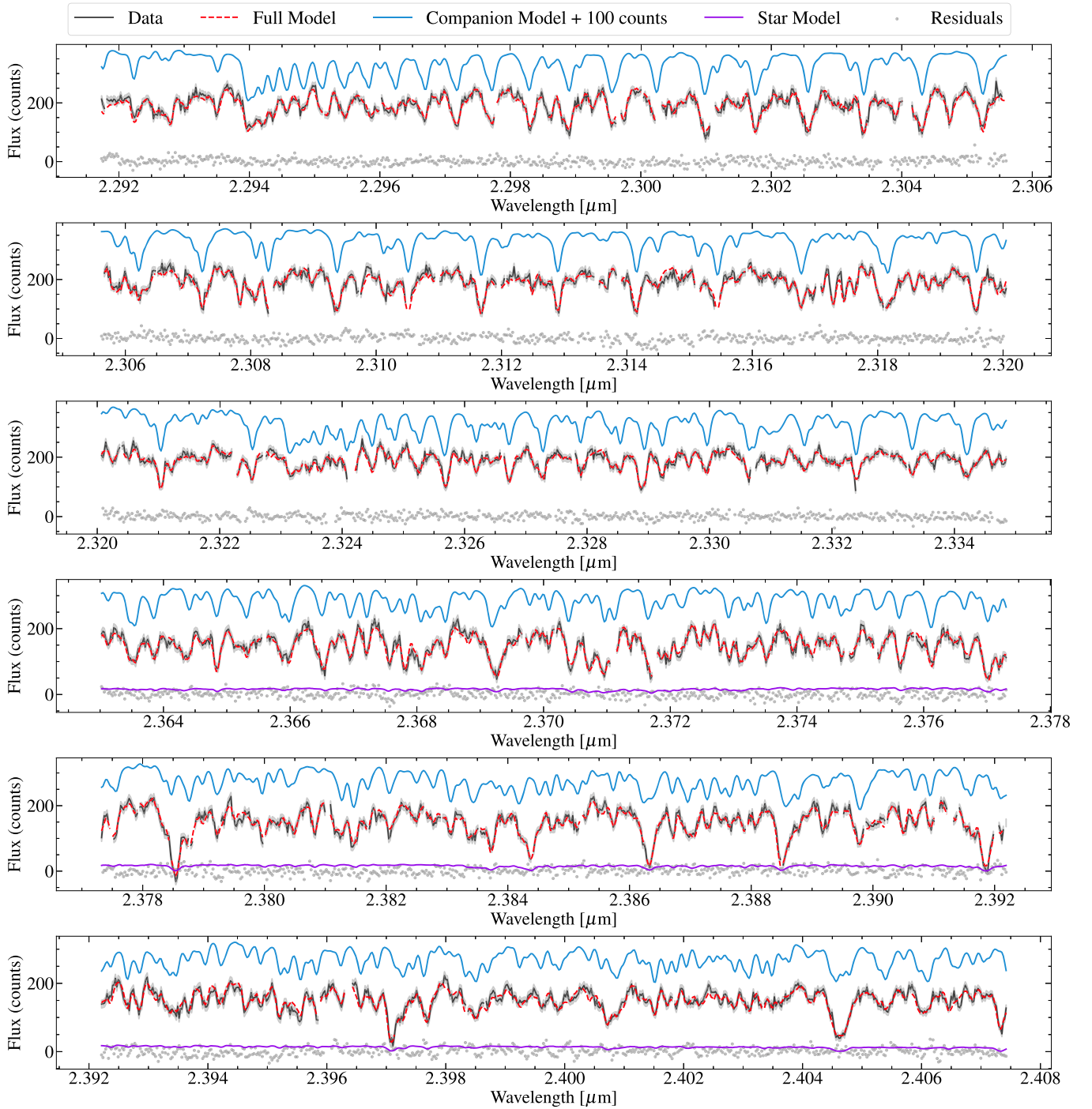


Figure 7. KPIC data (2023, fiber 2) for HIP 55507 B are plotted in black, with error bars in gray. We plot two out of three spectral orders (2.29–2.41 μm), and each order is broken into three panels. The full model (FM_B in Equation (1)) is in red and consists of the companion model (M_C) in blue, which has been RV-shifted and broadened; the stellar spectra (D_s) in purple to model the speckle contribution; and the telluric and instrumental response (T). The fringing model is also incorporated in the full model. The residuals are shown as gray points. For clarity, an offset of +100 counts was added to the companion model. The speckle contribution is small and consistent with zero for the first spectral order (top three panels), where we omitted the purple line.

7.2. HIP 55507 A

Using the higher-S/N spectra from 2023, we carry out retrievals with the sole goal of measuring isotopic abundances in HIP 55507 A. The best-fit model and stellar spectra are shown in Appendix F. We are able to measure $^{12}\text{CO}/^{13}\text{CO}$ and $\text{C}^{16}\text{O}/\text{C}^{18}\text{O}$ in the photosphere of the primary star. We add the

same 0.1 dex systematic error as we did for HIP 55507 B, resulting in $^{12}\text{CO}/^{13}\text{CO} = 79^{+21}_{-16}$ and $\text{C}^{16}\text{O}/\text{C}^{18}\text{O} = 288^{+125}_{-70}$.

In these HIP 55507 A retrievals, we assumed a fixed P - T profile ($T_{\text{eff}} = 4300$ K, $\log g = 4.5$). To assess the impact of this assumption on the resulting isotopic abundances, we repeated the fits with $T_{\text{eff}} = 4200$ and 4400 K P - T profiles

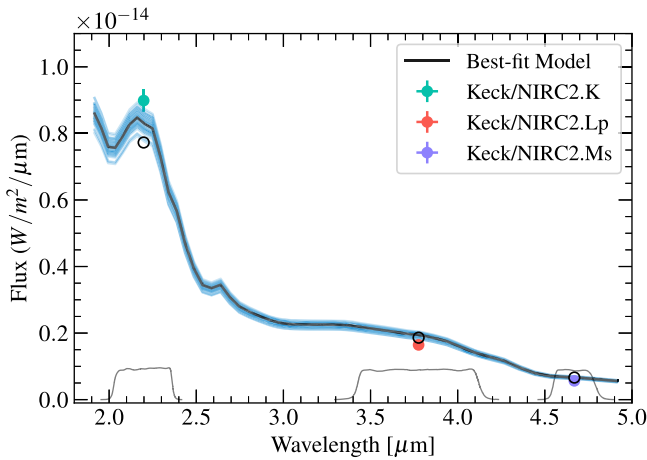


Figure 8. The photometry part of the retrieval for HIP 55507 B. The data are plotted in colored points, with filter transmission functions shown below. The best-fit model photometry points are shown in black open circles. The black curve is the best-fit spectra underlying the model photometry, while blue curves are random draws from the posterior.

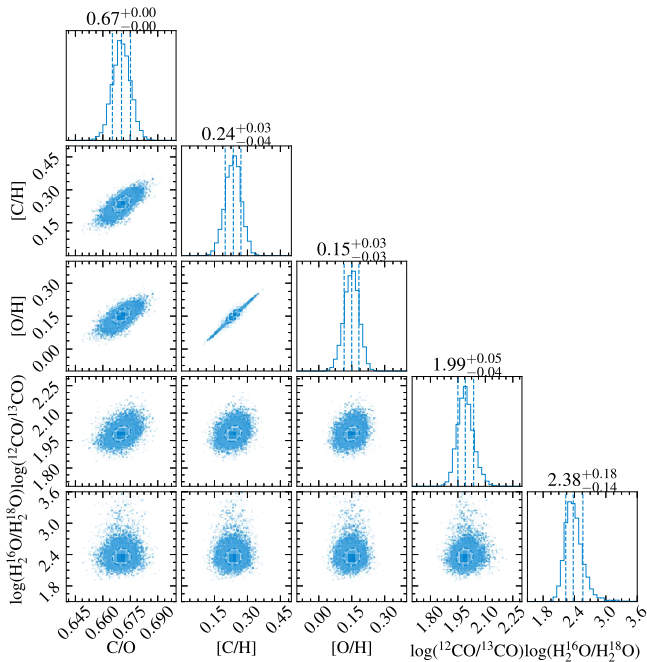


Figure 9. Posterior distributions for five key parameters from the baseline retrieval for HIP 55507 B. The titles on each histogram show the median and 68% credible interval. These represent the statistical errors, and we account for systematic errors in our reported values in Table 8. Note that [O/H] is not fitted in the retrievals but calculated from the C/O and [C/H] posteriors. The tight correlation between [C/H] and [O/H] indicates that KPIC high-resolution spectra can constrain relative abundances to much higher precision than absolute abundances, as found by previous high-resolution studies (Xuan et al. 2022; Finnerty et al. 2023).

(same $\log g$). We find that varying the P - T profile has little effect on the results; the posteriors shift by $<1\sigma$.

7.3. Relative RVs between HIP 55507 A and B

By combining the retrievals for HIP 55507 A and B, we compute the relative RV between the stars at the time of observation. The RV values corrected for barycentric motion are

provided in Appendix C. In both the 2021 and 2023 epochs, the stellar and companion RVs measured from fiber 3 are higher compared to those measured from fiber 2. This may be due to different RV zero-points for each fiber. To compute the relative RV, we subtract the stellar RV from the companion RV for each fiber separately and then take the average. For the 2023 epoch, the relative RV is consistent at the $<0.05 \text{ km s}^{-1}$ level between fibers. We conservatively adopt 0.1 km s^{-1} as the uncertainty. For the 2021 epoch, we adopt a larger uncertainty of 0.2 km s^{-1} , as the relative RV values disagree by $\sim 0.15 \text{ km s}^{-1}$ between fibers.

8. Discussion and Conclusions

8.1. Relative RVs and Dynamical Mass

In this paper, we demonstrate the value of relative RV data in orbit fits, which are uniquely enabled by direct measurements of the companion RV (Ruffio et al. 2019, 2023). When the primary star has sufficient absorption lines in the K band, as is the case for HIP 55507 A, we can directly measure the relative RV between the primary star and companion at the same epoch with Keck/KPIC. This measurement is powerful, since it is insensitive to potential systematics from zero-point offsets between the different instruments used to acquire the spectra. By including two epochs of KPIC relative RVs in our orbit fit for HIP 55507 AB, we find a 60% improvement in the dynamical mass measurement for HIP 55507 B ($88.0_{-3.2}^{+3.4} M_{\text{Jup}}$). Dynamical masses of low-mass companions are key measurements that allow us to test evolutionary and atmospheric models. Future work should explore whether relative RVs can also improve constraints on companion mass in systems with longer orbital separations (and therefore less orbital coverage), as many directly imaged companions have orbital separations $\gtrsim 100 \text{ au}$.

We note that our orbit solution for HIP 55507 AB also represents a significant improvement compared to those presented in Feng et al. (2022), who did not use relative astrometry data from imaging and only had access to the first 6.3 yr of HIRES RVs. Their derived orbital period of $14.0 \pm 1.4 \text{ yr}$ and companion mass of $5.0 \pm 0.6 M_{\text{Jup}}$ for HIP 55507 B are significantly discrepant from our results. Furthermore, the observed luminosity of the companion from our NIRC2 data is consistent with a low-mass star and not a $5.0 M_{\text{Jup}}$ planet (see Figure 4). In addition, we cannot reproduce their results even if we used the same data as Feng et al. (2022), namely, the first 6.3 yr of HIRES RVs and Gaia-Hipparcos absolute astrometry. In this case, our fits result in unbounded posteriors for mass and other orbital parameters (e.g., with a 1σ interval for semimajor axis from 13 to 840 au). We conclude that the choice of prior ranges in the orbit fit may be biasing the Feng et al. (2022) results for HIP 55507 B.

8.2. Isotopologue Ratios

Isotopologue ratios are thought to have implications for the formation pathway of planets and substellar companions, but our knowledge of how carbon and oxygen isotopic ratios relate to formation is still limited. We can benchmark the value of isotopologue measurements by using higher-mass brown dwarf and stellar companions that form via gravitational instability from a protostellar disk or molecular cloud. Because these

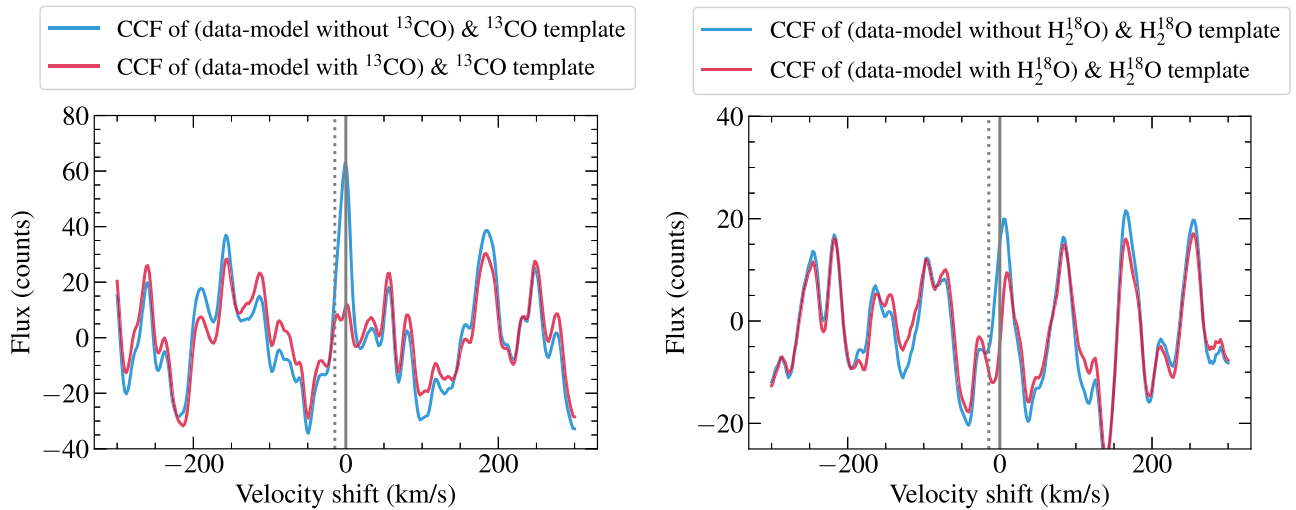


Figure 10. Left panel: the CCF between the ^{13}CO -only template and (data–best-fit model without ^{13}CO) in blue. The CCF between the ^{13}CO -only template and (data–best-fit model with ^{13}CO) is shown in red. The fact that the blue CCF shows a peak at the companion’s rest frame (gray solid line) indicates a real ^{13}CO detection. For comparison, the gray dotted line is the telluric rest frame. In the red CCF, we do not expect a peak, since ^{13}CO is fitted for in this model, so the residuals should be free of ^{13}CO . Right panel: same but for H_2^{18}O . The ^{13}CO signal is much clearer than the H_2^{18}O signal, which remains tentative at this stage.

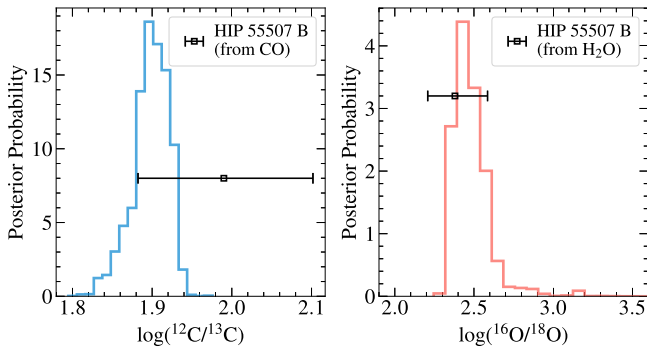


Figure 11. The posteriors for $\log(^{12}\text{CO}/^{13}\text{CO})$ and $\log(\text{C}^{16}\text{O}/\text{C}^{18}\text{O})$ measured from KPIC spectra of HIP 55507 A. We overplot the corresponding isotopic values measured with ^{13}CO for HIP 55507 B as error bars. Note that the $^{16}\text{O}/^{18}\text{O}$ constraint for HIP 55507 B is from $\log(\text{H}_2^{16}\text{O}/\text{H}_2^{18}\text{O})$.

systems are dominated by gas accretion, they should exhibit the same isotopic ratios between the primary and secondary components, which we can test observationally. To our knowledge, for main-sequence stellar binaries, this test has only been demonstrated once with an M dwarf binary system (Crossfield et al. 2019).

Using high-resolution spectra from Keck/KPIC ($R \sim 35,000$), we perform atmospheric retrievals for the M7.5 companion HIP 55507 B ($T_{\text{eff}} \sim 2400$ K) and its K6V primary star ($T_{\text{eff}} \sim 4300$ K). For HIP 55507 B, we retrieve $[\text{C}/\text{H}] = 0.24 \pm 0.13$ and $\text{C}/\text{O} = 0.67 \pm 0.04$. As shown in Figure 11, our measured $^{12}\text{CO}/^{13}\text{CO} = 98_{-22}^{+28}$ for HIP 55507 B is consistent to within 1σ with our measured $^{12}\text{CO}/^{13}\text{CO} = 79_{-16}^{+21}$ for the primary star under the assumption that HIP 55507 A and B share the same C/O and [C/H]. Furthermore, the $^{16}\text{O}/^{18}\text{O}$ measured from H_2O in HIP 55507 B is 240_{-80}^{+145} , consistent with the $^{16}\text{O}/^{18}\text{O} = 288_{-70}^{+125}$ measured from CO in HIP 55507 A. The agreement between $^{12}\text{C}/^{13}\text{C}$ and $^{16}\text{O}/^{18}\text{O}$ in the HIP 55507 AB system represents a rare test of chemical homogeneity for stellar binaries using isotopic ratios.

We note that our value of $\text{H}_2^{16}\text{O}/\text{H}_2^{18}\text{O} = 240_{-80}^{+145}$ for HIP 55507 B is lower by a factor of ~ 2 compared to the solar

value of 525 ± 21 (Lyons et al. 2018). A large difference between the $^{16}\text{O}/^{18}\text{O}$ in HIP 55507 AB and the Sun is not unexpected, as measurements of $^{16}\text{O}/^{18}\text{O}$ in molecular clouds at the solar galactocentric distance show a factor of ~ 3 scatter (Nittler & Gaidos 2012). Furthermore, studies of solar twins also reveal a wide range in $^{16}\text{O}/^{18}\text{O}$, with values as low as 50–100 (Coria et al. 2023). Given the tentative nature of the H_2^{18}O detection in HIP 55507 B, however, follow-up observations would be needed to confirm this measurement. In addition, our KPIC spectra for HIP 55507 B do not have sufficient S/N to constrain $\text{C}^{16}\text{O}/\text{C}^{18}\text{O}$ even if $\text{C}^{16}\text{O}/\text{C}^{18}\text{O} = \text{H}_2^{16}\text{O}/\text{H}_2^{18}\text{O}$ (see Section 6). Measuring $\text{C}^{16}\text{O}/\text{C}^{18}\text{O}$ in HIP 55507 B consistent with $\text{C}^{16}\text{O}/\text{C}^{18}\text{O}$ in the primary star would be a valuable test of our retrieval method and another piece of evidence supporting isotopic homogeneity between HIP 55507 A and B.

With a case study of the M7.5 companion HIP 55507 B using Keck/KPIC spectroscopy, we demonstrate the ability to measure carbon and oxygen elemental and isotopic abundances for late-M spectral types. In addition, we use KPIC to measure $^{12}\text{C}/^{13}\text{C}$ and $^{16}\text{O}/^{18}\text{O}$ for its K6V primary star and confirm that the companion and primary share the same isotopic abundances. While we made simplifications in our analysis of HIP 55507 A, future work with more extensive wavelength coverage (e.g., $H + K$ bands) could explore more sophisticated retrievals for late-K and early-M dwarf stars. Finally, the projected separation and flux ratio between HIP 55507 A and B are comparable to systems with young (~ 1 – 50 Myr) substellar companions of similar spectral types as HIP 55507 B ($T_{\text{eff}} \sim 2000$ – 2800 K), which opens the door to systematically measuring the elemental and isotopic abundances of these companions with KPIC.

Acknowledgments

J.X. thanks Paul Mollière for help with generating new opacities in `petitRADTRANS` and using `easyCHEM`. J.X. is supported by the NASA Future Investigators in NASA Earth and Space Science and Technology (FINESST) award No.

80NSSC23K1434. J.X. also acknowledges support from the Keck Visiting Scholars Program (KVSP) to commission KPIC Phase II capabilities. D.E. is supported by NASA FINESST award No. 80NSSC19K1423. D.E. also acknowledges support from the Keck Visiting Scholars Program (KVSP) to install the Phase II upgrades. Funding for KPIC has been provided by the California Institute of Technology, the Jet Propulsion Laboratory, the Heising–Simons Foundation (grant Nos. 2015-129, 2017-318, 2019-1312, and 2023-4598), the Simons Foundation, and the NSF under grant AST-1611623. The computations presented here were conducted at the Resnick High Performance Center, a facility supported by the Resnick Sustainability Institute at the California Institute of Technology. W. M. Keck Observatory access was supported by Northwestern University and the Center for Interdisciplinary Exploration and Research in Astrophysics (CIERA). This research has made use of the Keck Observatory Archive (KOA), which is operated by the W. M. Keck Observatory and the NASA Exoplanet Science Institute (NExSci), under contract with the National Aeronautics and Space Administration. The data presented herein were obtained at the W. M. Keck Observatory, which is operated as a scientific partnership among the California Institute of Technology, the University of California, and the National Aeronautics and Space Administration. The Observatory was made possible by the generous financial support of the W. M. Keck Foundation. The authors wish to recognize and acknowledge the very significant cultural role and reverence that the summit of Maunakea has always had within the indigenous Hawaiian community. We are most fortunate to have the opportunity to conduct observations from this mountain.

Facility: Keck:II (KPIC).

Software: `petitRADTRANS` (Mollière et al. 2019), `dynesty` (Speagle 2020), `species` (Stolker et al. 2020).

Appendix A HIRES RVs for HIP 55507 A

The Keck/HIRES RVs for HIP 55507 A used in the orbit fits are provided in Table A1.

Table A1
HIRES RV Measurements for HIP 55507 A

Epoch (JD)	RV (m s^{-1})	RV Error (m s^{-1})
2454928.956275	−85.2891389311628	1.30891144275665
2455164.14972	−68.7729316154637	1.47898721694946
2455188.145761	−66.6667559203668	1.43427407741547
2455191.15537	−75.0535222054357	1.24979019165039
2455232.042467	−62.6764906469445	1.54032349586487
2455255.95588	−72.1607865157624	1.34993493556976
2455260.916671	−54.8581642759654	1.45500349998474
2455285.96214	−59.8329068133204	1.38776302337646
2455342.836003	−53.2058373492368	1.31268215179443
2455343.8461	−57.5779338603028	1.33945858478546
2455344.865259	−48.9945473322775	1.58772456645966
2455373.79232	−62.9124972583049	1.31496453285217
2455376.787806	−63.2145698783239	1.29381465911865
2455395.813169	−50.7233486928718	1.46614670753479
2455399.805149	−54.886460583263	1.60360312461853
2455557.052607	−52.3534558265392	1.37891674041748
2455614.102829	−43.3644036486916	1.48802018165588
2455635.058738	−34.5544936031586	1.8173508644104
2455663.95977	−44.8672651793666	1.25698328018188
2455668.877009	−40.9864458731045	1.30355906486511
2455670.931216	−42.3292736833009	1.37228858470917
2456320.142426	16.0774879418836	1.54433631896973
2456327.067151	7.77230437090594	1.60971903800964
2456450.81181	0.541037387102907	1.27542078495026
2457201.75372	49.0106801572104	1.33652639389038
2459373.76488	159.649231940397	1.27313685417175
2459541.113394	168.07387611986	1.4402596950531
2459546.067624	180.157805514196	1.30128860473633
2459592.990193	189.869930526855	1.37484121322632
2460094.770983	199.762668142396	1.5842090845108
2460104.749802	200.888299897594	1.35568201541901

Appendix B NIRC2 Imaging and Orbit Fits for HIP 55507 AB

We show an example pyklip fit of Keck/NIRC2 data in Figure B1, and provide plots from the orbit fit in Figure B2.

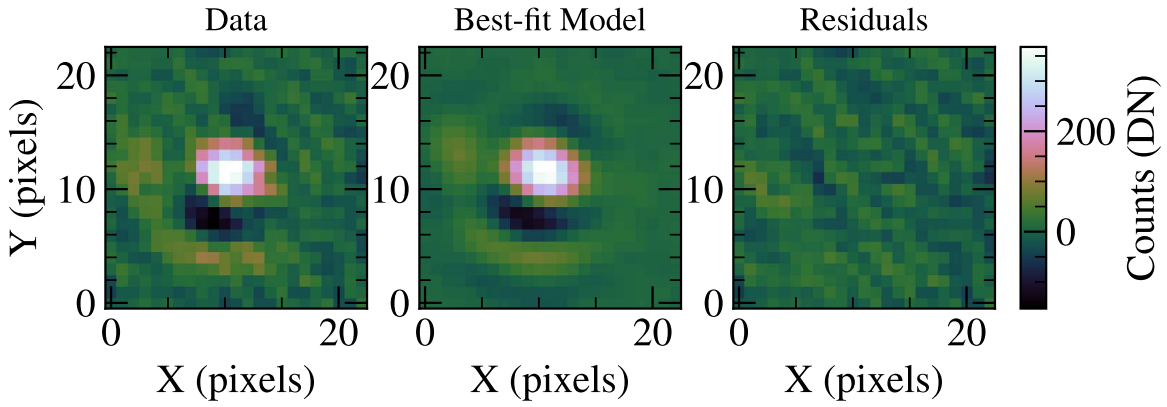


Figure B1. An example `pyklip` fit for the NIRC2 imaging data from UT 2022 June 9 with the *K* filter. The companion PSF after ADI is shown in the left panel, the forward model in the middle panel, and residuals in the right panel.

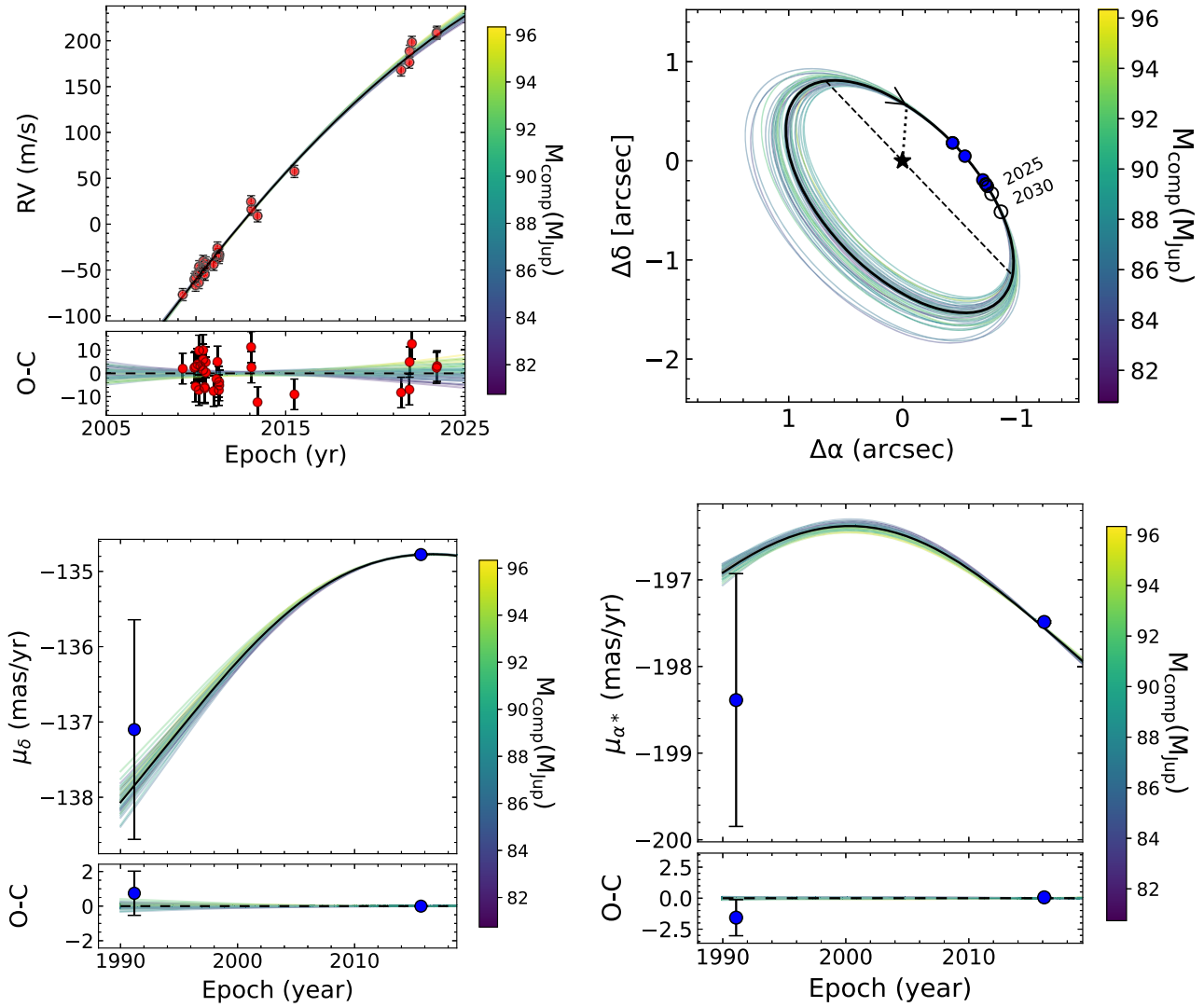


Figure B2. Results from the orbit fit using host star RV (top left), relative astrometry (top right), absolute astrometry from Gaia and Hipparcos (bottom panels), and relative RVs from KPIC (shown in Figure 2). The orbit fit is performed with the `orvara` package (Brandt et al. 2021). The random draws from the posterior are color-coded by the companion mass.

Appendix C KPIC RVs for HIP 55507 AB

We list Keck/KPIC RVs for both HIP 55507 A and B in Table C1.

Table C1
RV Measurements for HIP 55507 A and B from KPIC

UT Date	Object	BJD–2400000	SF2 RV (km s ⁻¹)	SF3 RV (km s ⁻¹)
2021 Jul 4	HIP 55507 A	59399.73	-5.48 ± 0.03	-5.38 ± 0.03
2021 Jul 4	HIP 55507 B	59399.73	-7.33 ± 0.06	-7.08 ± 0.07
Relative RV = -1.78 ± 0.20 km s ⁻¹				
2023 May 2	HIP 55507 A	60066.78	-5.47 ± 0.02	-5.15 ± 0.02
2023 May 2	HIP 55507 B	60066.78	-7.31 ± 0.05	-7.03 ± 0.06
Relative RV = -1.86 ± 0.10 km s ⁻¹				

Note. We have applied the barycentric correction to the individual RVs for A and B, so their reference is the solar system barycenter. The relative RV is defined as $RV_B - RV_A$. For the relative RV values, we inflated the errors to account for systematics between fibers.

Appendix D Fringing Model for KPIC

We identified three sources of fringing in KPIC data: two dichroics in KPIC and optics in the NIRSPEC entrance window (Finnerty et al. 2022). One of the two dichroics in particular causes the fringing signal to change when we switch from observing the primary star to observing an off-axis companion, as this dichroic is directly downstream of our fiber-injection-unit tip-tilt mirror, which steers the light of either the star or companion in the fiber. When the tip-tilt mirror switches from the on-axis star to the off-axis companion, the angle of incidence of light into the dichroic changes, which causes the fringing signal to change. The change in modulation, t , as light passes through a transmissive optic is described by the well-known formula

$$t = \left[1 + F \sin^2 \left(\frac{2\pi n l \cos(\theta)}{\lambda} \right) \right]^{-1}. \quad (\text{D1})$$

Here, $F = 4R/(1-R)^2$, where R is the reflectivity of the material; n is the index of refraction of the material, which depends on temperature and wavelength; l is the thickness of the material; θ is the angle of incidence into the material; and λ is the wavelength of light. All KPIC observations to date have spectra affected by three fringing modulation terms multiplied in series, but two of them are expected to be relatively static when going from star observations to companion observations.

We fit the fringing signal in these spectra with a simplified approximation where the companion observations experience an additional modulation term as compared to the star observations. We also simplify the above equation to

$$t' = \left[1 + F \sin^2 \left(\frac{2\pi n(T_d, \lambda) \times d}{\lambda} \right) \right]^{-1}. \quad (\text{D2})$$

We multiply t' onto the spectral response (i.e., T in Equations (1) and (2)) to match the fringing in the observed

spectra for both HIP 55507 A and B. We fit for three parameters per spectral order: an optical path length (d) term that combines both the thickness of the glass and the angle of incidence, the fractional amplitude of the ghost from the dichroics (F), and the temperature of the dichroics (T_d) that governs the index of refraction. To model the CaF₂ dichroic, we used the Sellmeier coefficients reported by Leviton et al. (2007) to determine how the index of refraction changes with wavelength and temperature. Each science fiber is treated separately, as the fringing is different in each due to different angles of incidence.

Appendix E Fitting HIP 55507 A Spectra with PHOENIX-ACES Models

We fit the HIP 55507 A spectra using PHOENIX-ACES models (Husser et al. 2013) to measure RV , T_{eff} , and $\log g$. Our grid of PHOENIX-ACES models assumes solar metallicity and has 100 K spacing in T_{eff} and 0.5 dex spacing in $\log g$. The forward model and fringing model used for this fit are described in Section 5.1.

From these fits, we obtain a fairly consistent picture of T_{eff} and $\log g$ between the different observation epochs. Our statistical errors on each measured T_{eff} and $\log g$ are very small: ~ 15 K for T_{eff} and 0.01 dex for $\log g$. In reality, model uncertainties are expected to be larger, so we report the weighted averages and adopt half a grid step as the error bars. In summary, we find $T_{\text{eff}} = 4200 \pm 50$ K and $\log g = 4.40 \pm 0.25$, which agree within 1σ with the literature values listed in Table 1.

Appendix F Fitting HIP 55507 A Spectra with petitRADTRANS

We show the best-fit petitRADTRANS model and HIP 55507 A spectra in Figure F1.

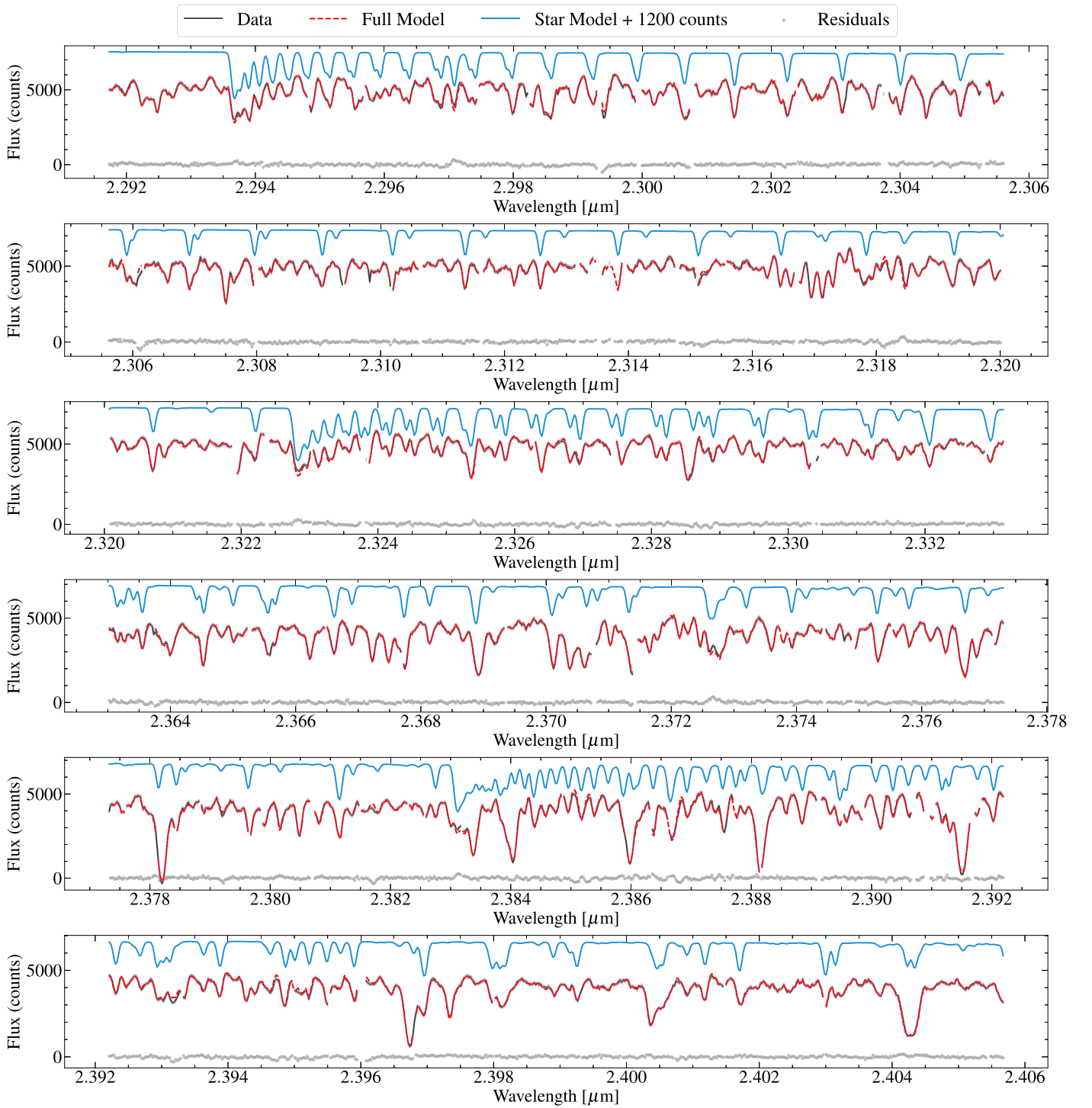


Figure F1. KPIC spectra for HIP 55507 A are plotted in black. We break up each spectral order into three panels. The full model (FM_A in Equation (2)) is in red and includes the stellar model (M_A) from `petitRADTRANS` in blue and the telluric and instrumental response (T). The fringing model is also incorporated in the full model. The stellar model is offset by +1200 counts for clarity. The residuals are shown as gray points. CO lines dominate at these wavelengths for HIP 55507 A. We measure $^{12}\text{CO}/^{13}\text{CO}$ and $\text{C}^{16}\text{O}/\text{C}^{18}\text{O}$ from the spectrum.

ORCID iDs

Jerry W. Xuan <https://orcid.org/0000-0002-6618-1137>
 Jason Wang <https://orcid.org/0000-0003-0774-6502>
 Luke Finnerty <https://orcid.org/0000-0002-1392-0768>
 Anne E. Peck <https://orcid.org/0000-0003-2461-6881>
 Eric Nielsen <https://orcid.org/0000-0001-6975-9056>
 Heather A. Knutson <https://orcid.org/0000-0002-5375-4725>

Howard Isaacson <https://orcid.org/0000-0002-0531-1073>
 Andrew W. Howard <https://orcid.org/0000-0001-8638-0320>
 Michael C. Liu <https://orcid.org/0000-0003-2232-7664>
 Sam Walker <https://orcid.org/0000-0001-7062-815X>
 Jean-Baptiste Ruffio <https://orcid.org/0000-0003-2233-4821>

Yapeng Zhang  <https://orcid.org/0000-0003-0097-4414>
 Julie Inglis  <https://orcid.org/0000-0001-9164-7966>
 Nicole L. Wallack  <https://orcid.org/0000-0003-0354-0187>
 Aniket Sanghi  <https://orcid.org/0000-0002-1838-4757>
 Erica J. Gonzales  <https://orcid.org/0000-0002-9329-2190>
 Fei Dai  <https://orcid.org/0000-0002-8958-0683>
 Marta L. Bryan  <https://orcid.org/0000-0002-6076-5967>
 Benjamin Calvin  <https://orcid.org/0000-0003-4737-5486>
 Jacques-Robert Delorme  <https://orcid.org/0000-0001-8953-1008>
 Michael P. Fitzgerald  <https://orcid.org/0000-0002-0176-8973>
 Nemanja Jovanovic  <https://orcid.org/0000-0001-5213-6207>
 Joshua Liberman  <https://orcid.org/0000-0002-4934-3042>
 Ronald A. López  <https://orcid.org/0000-0002-2019-4995>
 Emily C. Martin  <https://orcid.org/0000-0002-0618-5128>
 Garreth Ruane  <https://orcid.org/0000-0003-4769-1665>
 Ben Sappey  <https://orcid.org/0000-0003-1399-3593>
 Andrew Skemer  <https://orcid.org/0000-0001-6098-3924>
 J. Kent Wallace  <https://orcid.org/0000-0001-5299-6899>
 Ji Wang  <https://orcid.org/0000-0002-4361-8885>
 Yinzi Xin  <https://orcid.org/0000-0002-6171-9081>
 Shubh Agrawal  <https://orcid.org/0000-0003-2429-5811>
 Clarissa R. Do Ó  <https://orcid.org/0000-0001-5173-2947>
 Chih-Chun Hsu  <https://orcid.org/0000-0002-5370-7494>
 Caprice L. Phillips  <https://orcid.org/0000-0001-5610-5328>

References

- Ackerman, A. S., & Marley, M. S. 2001, *ApJ*, 556, 872
 Allard, F., Hauschildt, P. H., Alexander, D. R., Tamanai, A., & Schweitzer, A. 2001, *ApJ*, 556, 357
 Anders, F., Khalatyan, A., Queiroz, A. B., et al. 2022, *A&A*, 658, A91
 Asplund, M., Grevesse, N., Sauval, A. J., & Scott, P. 2009, *ARA&A*, 47, 481
 Azzam, A. A., Tennyson, J., Yurchenko, S. N., & Naumenko, O. V. 2016, *MNRAS*, 460, 4063
 Baraffe, I., Homeier, D., Allard, F., & Chabrier, G. 2015, *A&A*, 577, A42
 Bernath, P. F. 2020, *JQSRT*, 240, 106687
 Biller, B. A., Liu, M. C., Wahhaj, Z., et al. 2010, *ApJL*, 720, L82
 Botelho, R. B., Milone, A. d. C., Meléndez, J., et al. 2020, *MNRAS*, 499, 2196
 Bouma, L. G., Palumbo, E. K., & Hillenbrand, L. A. 2023, *ApJL*, 947, L3
 Brandt, T. D. 2021, *ApJS*, 254, 42
 Brandt, T. D., Dupuy, T. J., Li, Y., et al. 2021, *AJ*, 162, 186
 Brooke, J. S., Bernath, P. F., Western, C. M., et al. 2016, *JQSRT*, 168, 142
 Brown-Sevilla, S. B., Maire, A. L., Mollière, P., et al. 2023, *A&A*, 673, A98
 Burningham, B., Marley, M. S., Line, M. R., et al. 2017, *MNRAS*, 470, 1177
 Butler, R. P., Marcy, G. W., Williams, E., et al. 1996, *PASP*, 108, 500
 Calahan, J. K., Bergin, E. A., & Bosman, A. D. 2022, *ApJL*, 934, L14
 Carvalho, A., & Johns-Krull, C. M. 2023, *RNAAS*, 7, 91
 Chachan, Y., Knutson, H. A., Lothringer, J., & Blake, G. A. 2023, *ApJ*, 943, 112
 Christiaens, V., Gonzalez, C., Farkas, R., et al. 2023, *JOSS*, 8, 4774
 Coria, D. R., Crossfield, I. J. M., Lothringer, J., et al. 2023, *ApJ*, 954, 121
 Cridland, A. J., Dishoeck, E. F. V., Alessi, M., & Pudritz, R. E. 2020, *A&A*, 642, A229
 Crossfield, I. J. M., Lothringer, J. D., Flores, B., et al. 2019, *ApJL*, 871, L3
 Cutri, R. M., Skrutskie, M. F., van Dyk, S., et al. 2003, VizieR Online Data Catalog: 2MASS All-Sky Catalog of Point Sources II/246
 Cutri, R. M., Wright, E. L., Conrow, T., et al. 2021, VizieR Online Data Catalog: AllWISE Data Release II/328
 Czesla, S., Schröter, S., Schneider, C. P., et al., 2019 PyA: Python Astronomy-related Packages, Astrophysics Source Code Library, ascl:1906.010
 Delorme, J.-R., Jovanovic, N., Echeverri, D., et al. 2021, *JATIS*, 7, 035006
 Do Ó, C. R., O’Neil, K. K., Konopacky, Q. M., et al. 2023, *AJ*, 166, 48
 Dulick, M., Bauschlicher, C. W., Jr., Burrows, A., et al. 2003, *ApJ*, 594, 651
 Dupuy, T. J., & Liu, M. C. 2012, *ApJS*, 201, 19
 Dupuy, T. J., Liu, M. C., Bowler, B. P., et al. 2010, *ApJ*, 721, 1725
 Echeverri, D., Jovanovic, N., Delorme, J.-R., et al. 2022, *Proc. SPIE*, 12184, 121841W
 Feng, F., Butler, R. P., Vogt, S. S., et al. 2022, *ApJS*, 262, 21
 Finnerty, L., Schofield, T., Delorme, J.-R., et al. 2022, *Proc. SPIE*, 12184, 121844Y
 Finnerty, L., Schofield, T., Sappey, B., et al. 2023, *AJ*, 166, 31
 Founesneau, M., Andrae, R., Dharmawardena, T., et al. 2022, *A&A*, 662, A125
 Franson, K., Bowler, B. P., Bonavita, M., et al. 2023, *AJ*, 165, 39
 Gaia Collaboration, Brown, A. G. A., Vallenari, A., et al. 2018, *A&A*, 616, A1
 Gaia Collaboration, Vallenari, A., Brown, A. G. A., et al. 2023, *A&A*, 674, A1
 Gaidos, E., Fischer, D. A., Mann, A. W., & Howard, A. W. 2013, *ApJ*, 771, 18
 Gillon, M., Jehin, E., Lederer, S. M., et al. 2016, *Natur*, 533, 221
 Gomez Gonzalez, C. A., Wertz, O., Absil, O., et al. 2017, *AJ*, 154, 7
 Gonzales, E. C., Burningham, B., Faherty, J. K., et al. 2022, *ApJ*, 938, 56
 Gonzales, E. J., Crepp, J. R., Bechter, E. B., et al. 2020, *ApJ*, 893, 27
 Grimm, S. L., & Heng, K. 2015, *ApJ*, 808, 182
 Grimm, S. L., Malik, M., Kitzmann, D., et al. 2021, *ApJS*, 253, 30
 Grootel, V. V., Fernandes, C. S., Gillon, M., et al. 2018, *ApJ*, 853, 30
 Hejazi, N., Crossfield, I. J. M., Nordlander, T., et al. 2023, *ApJ*, 949, 79
 Hood, C. E., Fortney, J. J., Line, M. R., & Faherty, J. K. 2023, *ApJ*, 953, 170
 Horne, K. 1986, *PASP*, 98, 609
 Howard, A. W., Johnson, J. A., Marcy, G. W., et al. 2010, *ApJ*, 721, 1467
 Husser, T.-O., Berg, S. W.-v., Dreizler, S., et al. 2013, *A&A*, 553, A6
 Iyer, A. R., Line, M. R., Muirhead, P. S., Fortney, J. J., & Gharib-Nezhad, E. 2023, *ApJ*, 944, 41
 Kurucz, R. L. 2011, *CaJPh*, 89, 417
 Leggett, S. K., Currie, M. J., Varricatt, W. P., et al. 2006, *MNRAS*, 373, 781
 Leviton, D. B., Frey, B. J., & Madison, T. J. 2007, *Proc. SPIE*, 6692, 669204
 Lightkurve Collaboration, Cardoso, J. V. D. M., Hedges, C., et al., 2018 Lightkurve: Kepler and TESS Time Series Analysis in Python, Astrophysics Source Code Library, ascl:1812.013
 Lindegren, L., Bastian, U., Biermann, M., et al. 2021, *A&A*, 649, A4
 Line, M. R., Brogi, M., Bean, J. L., et al. 2021, *Natur*, 598, 580
 Liu, M. C. 2004, *Sci*, 305, 1442
 Lueber, A., Kitzmann, D., Bowler, B. P., Burgasser, A. J., & Heng, K. 2022, *ApJ*, 930, 136
 Lyons, J. R., Gharib-Nezhad, E., & Ayres, T. R. 2018, *NatCo*, 9, 908
 Maire, A. L., Bonnefoy, M., Ginski, C., et al. 2016, *A&A*, 587, A56
 Marois, C., Lafrenière, D., Doyon, R., Macintosh, B., & Nadeau, D. 2006, *ApJ*, 641, 556
 Martin, E. C., Fitzgerald, M. P., McLean, I. S., et al. 2018, *Proc. SPIE*, 10702, 107020A
 Mawet, D., Ruane, G., Xuan, W., et al. 2017, *ApJ*, 838, 92
 McKemmish, L. K., Masseron, T., Hoeijmakers, H. J., et al. 2019, *MNRAS*, 488, 2836
 McKemmish, L. K., Yurchenko, S. N., & Tennyson, J. 2016, *MNRAS*, 463, 771
 Mollière, P., Molyarova, T., Bitsch, B., et al. 2022, *ApJ*, 934, 74
 Mollière, P., & Snellen, I. A. 2019, *A&A*, 622, A139
 Mollière, P., Stolker, T., Lacour, S., et al. 2020, *A&A*, 640, A131
 Mollière, P., Wardenier, J. P., van Boekel, R., et al. 2019, *A&A*, 627, A67
 Morley, C. V., Skemer, A. J., Miles, B. E., et al. 2019, *ApJL*, 882, L29
 Nittler, L. R., & Gaidos, E. 2012, *MAPS*, 47, 2031
 Öberg, K. I., Facchini, S., & Anderson, D. E. 2023, *ARA&A*, 61, 287
 Petigura, E. A. 2015, PhD thesis, Univ. California, Berkeley
 Piette, A. A. A., & Madhusudhan, N. 2020, *MNRAS*, 497, 5136
 Polyansky, O. L., Kyuberis, A. A., Lodi, L., et al. 2017, *MNRAS*, 466, 1363
 Polyansky, O. L., Kyuberis, A. A., Zobov, N. F., et al. 2018, *MNRAS*, 480, 2597
 Pueyo, L. 2016, *ApJ*, 824, 117
 Redai, J. I. A., Follette, K. B., Wang, J., et al. 2023, *AJ*, 165, 57
 Robichaud, J. L., Zellers, B., Philippon, R., McLean, I. S., & Figer, D. F. 1998, *Proc. SPIE*, 3354, 1068
 Romano, D., Matteucci, F., Zhang, Z. Y., Papadopoulos, P. P., & Ivison, R. J. 2017, *MNRAS*, 470, 401
 Rothman, L. S., Gordon, I. E., Barber, R. J., et al. 2010, *JQSRT*, 111, 2139
 Rowland, M. J., Morley, C. V., & Line, M. R. 2023, *ApJ*, 947, 6
 Ruffio, J.-B., Horstman, K., Mawet, D., et al. 2023, *AJ*, 165, 113
 Ruffio, J.-B., Macintosh, B., Konopacky, Q. M., et al. 2019, *AJ*, 158, 200
 Sanghi, A., Liu, M. C., Best, W. M., et al. 2023, *ApJ*, 959, 63
 Schwarz, H., Ginski, C., de Kok, R. J., et al. 2016, *A&A*, 593, A74
 Sebastian, D., Gillon, M., Ducrot, E., et al. 2021, *A&A*, 645, A100
 Service, M., Lu, J. R., Campbell, R., et al. 2016, *PASP*, 128, 095004
 Soummer, R., Pueyo, L., & Larkin, J. 2012, *ApJL*, 755, L28
 Speagle, J. S. 2020, *MNRAS*, 493, 3132

- Stanford-Moore, S. A., Nielsen, E. L., Rosa, R. J. D., Macintosh, B., & Czekala, I. 2020, *ApJ*, **898**, 27
- Stassun, K. G., Oelkers, R. J., Paegert, M., et al. 2019, *AJ*, **158**, 138
- Stolker, T., Quanz, S. P., Todorov, K. O., et al. 2020, *A&A*, **635**, A182
- Trotta, R. 2008, *ConPh*, **49**, 71
- Turrini, D., Schisano, E., Fonte, S., et al. 2021, *ApJ*, **909**, 40
- Vogt, S. S., Allen, S. L., Bigelow, B. C., et al. 1994, *Proc. SPIE*, **2198**, 362
- Wakeford, H. R., & Sing, D. K. 2015, *A&A*, **573**, A122
- Wang, J., Kolecki, J. R., Ruffio, J.-B., et al. 2022, *AJ*, **163**, 189
- Wang, J. J., Graham, J. R., Pueyo, L., et al. 2016, *AJ*, **152**, 97
- Wang, J. J., Ruffio, J.-B., De Rosa, R. J., et al., 2015 pyKLIP: PSF Subtraction for Exoplanets and Disks, Astrophysics Source Code Library, ascl:1506.001
- Wang, J. J., Ruffio, J.-B., Morris, E., et al. 2021, *AJ*, **162**, 148
- Wang, S.-i., Hildebrand, R. H., Hobbs, L. M., et al. 2003, *Proc. SPIE*, **4841**, 1145
- Whiteford, N., Glasse, A., Chubb, K. L., et al. 2023, *MNRAS*, **525**, 1375
- Wilson, T. L. 1999, *RPPh*, **62**, 143
- Xuan, J. W., Wang, J., Ruffio, J.-B., et al. 2022, *ApJ*, **937**, 54
- Xuan, W. J., Mawet, D., Ngo, H., et al. 2018, *AJ*, **156**, 156
- Yee, S. W., Petigura, E. A., & von Braun, K. 2017, *ApJ*, **836**, 77
- Yelda, S., Lu, J. R., Ghez, A. M., et al. 2010, *ApJ*, **725**, 331
- Yurchenko, S. N., Williams, H., Leyland, P. C., Lodi, L., & Tennyson, J. 2018, *MNRAS*, **479**, 1401
- Zhang, Y., Snellen, I. A. G., Bohn, A. J., et al. 2021a, *Natur*, **595**, 370
- Zhang, Y., Snellen, I. A. G., & Mollière, P. 2021b, *A&A*, **656**, A76